



Characterization of the strain-rate-dependent mechanical response of single cell–cell junctions

Amir Monemian Esfahani^a, Jordan Rosenbohm^a, Bahareh Tajvidi Safa^a, Nickolay V. Lavrik^{b,1}, Grayson Minnick^a, Quan Zhou^c, Fang Kong^d, Xiaowei Jin^a, Eunju Kim^a, Ying Liu^e, Yongfeng Lu^{a,e}, Jung Yul Lim^a, James K. Wahl III^f, Ming Dao^{g,1}, Changjin Huang^{c,h,1}, and Ruiguo Yang^{a,i,j,1}

^aDepartment of Mechanical and Materials Engineering, University of Nebraska–Lincoln, Lincoln, NE 68516; ^bCenter for Nanophase Materials Sciences, Oak Ridge National Laboratory, Oak Ridge, TN 37831-6054; ^cSchool of Mechanical and Aerospace Engineering, Nanyang Technological University, 639798 Singapore, Republic of Singapore; ^dSchool of Biological Sciences, Nanyang Technological University, 637551 Singapore, Republic of Singapore; ^eDepartment of Electrical and Computer Engineering, University of Nebraska–Lincoln, Lincoln, NE 68516; ^fDepartment of Oral Biology, University of Nebraska Medical Center, Lincoln, NE 68583; ^gDepartment of Materials Science and Engineering, Massachusetts Institute of Technology, Cambridge, MA 02139; ^hSchool of Chemical and Biomedical Engineering, Nanyang Technological University, 637459 Singapore, Republic of Singapore; ⁱNebraska Center for Integrated Biomolecular Communication, University of Nebraska–Lincoln, Lincoln, NE 68588; and ^jMary and Dick Holland Regenerative Medicine Program, University of Nebraska Medical Center, Omaha, NE 68198

Edited by David A. Weitz, Harvard University, Cambridge, MA, and approved December 27, 2020 (received for review September 14, 2020)

Cell–cell adhesions are often subjected to mechanical strains of different rates and magnitudes in normal tissue function. However, the rate-dependent mechanical behavior of individual cell–cell adhesions has not been fully characterized due to the lack of proper experimental techniques and therefore remains elusive. This is particularly true under large strain conditions, which may potentially lead to cell–cell adhesion dissociation and ultimately tissue fracture. In this study, we designed and fabricated a single-cell adhesion micro tensile tester (SCAμTT) using two-photon polymerization and performed displacement-controlled tensile tests of individual pairs of adherent epithelial cells with a mature cell–cell adhesion. Straining the cytoskeleton–cell adhesion complex system reveals a passive shear-thinning viscoelastic behavior and a rate-dependent active stress-relaxation mechanism mediated by cytoskeleton growth. Under low strain rates, stress relaxation mediated by the cytoskeleton can effectively relax junctional stress buildup and prevent adhesion bond rupture. Cadherin bond dissociation also exhibits rate-dependent strengthening, in which increased strain rate results in elevated stress levels at which cadherin bonds fail. This bond dissociation becomes a synchronized catastrophic event that leads to junction fracture at high strain rates. Even at high strain rates, a single cell–cell junction displays a remarkable tensile strength to sustain a strain as much as 200% before complete junction rupture. Collectively, the platform and the biophysical understandings in this study are expected to build a foundation for the mechanistic investigation of the adaptive viscoelasticity of the cell–cell junction.

cell mechanics | cell–cell junction | stress–strain relationship | stress relaxation

Adhesive organelles between neighboring epithelial cells form an integrated network as the foundation of complex tissues (1). As part of normal physiology, this integrated network is constantly exposed to mechanical stress and strain, which is essential to normal cellular activities, such as proliferation (2–4), migration (5, 6), differentiation (7), and gene regulation (7, 8) associated with a diverse set of functions in tissue morphogenesis (9–11) and wound healing (9). A host of developmental defects or clinical pathologies in the form of compromised cell–cell associations will arise when cells fail to withstand external mechanical stress due to genetic mutations or pathological perturbations (12, 13). Indeed, since the mechanical stresses are mainly sustained by the intercellular junctions, which may represent the weakest link and limit the stress tolerance within the cytoskeleton network of a cell sheet, mutations or disease-induced changes in junction molecules and components in adherens junctions and desmosomes lead to cell layer fracture and tissue fragility, which exacerbate the pathological conditions

(14–17). This clinical relevance gives rise to the importance of understanding biophysical transformations of the cell–cell adhesion interface when cells are subjected to mechanical loads.

As part of their normal functions, cells often experience strains of tens to a few hundred percent at strain rates of 10^{-4} to 1 s^{-1} (18–21). For instance, embryonic epithelia are subjected to strain rates in the range of 10^{-4} to 10^{-3} s^{-1} during normal embryogenesis (22). Strain rates higher than 0.1 s^{-1} are often experienced by adult epithelia during various normal physiological functions (21, 23, 24), such as breathing motions in the lung (1 to 10 s^{-1}) (25), cardiac pulses in the heart (1 to 6.5 s^{-1}) (20), peristaltic movements in the gut (0.4 to 1.5 s^{-1}), and normal stretching of the skin (0.1 to 5 s^{-1}). Cells have different mechanisms to dissipate the internal stress produced by external strain to avoid fracture, often via cytoskeleton remodeling and cell–cell adhesion enhancement (26, 27). These coping mechanisms may have different characteristic timescales. Cytoskeleton remodeling can dissipate mechanical stress promptly due to its viscoelastic

Significance

Cell–cell junctions are essential components in multicellular structures and often experience strains of different magnitudes and rates. However, their mechanical behavior is currently underexplored due to the lack of techniques to quantitatively characterize junctional stress–strain relationships. We developed a polymeric microstructure to strain the mutual junction of a single cell pair while simultaneously recording the junction stress and observed previously unseen strain-rate-dependent junction responses. We showed that cytoskeleton growth could relax the stress buildup and prevent junction failure at low strain rates, while high strain rates led to synchronized junction failures at remarkably large strains (over 200%). We expect this platform and our biophysical understanding to form the foundation for the rate-dependent mechanics of cell–cell junctions.

Author contributions: M.D., C.H., and R.Y. designed research; A.M.E., J.R., B.T.S., N.V.L., G.M., Q.Z., F.K., X.J., E.K., Y. Liu, Y. Lu, J.Y.L., J.K.W., and C.H. performed research; A.M.E., J.R., B.T.S., G.M., Q.Z., and F.K. analyzed data; and A.M.E., J.R., M.D., C.H., and R.Y. wrote the paper.

The authors declare no competing interest.

This article is a PNAS Direct Submission.

Published under the PNAS license.

¹To whom correspondence may be addressed. Email: lavriknv@ornl.gov, mingdao@MIT.EDU, cjuang@ntu.edu.sg, or ryang6@unl.edu.

This article contains supporting information online at <https://www.pnas.org/lookup/suppl/doi:10.1073/pnas.2019347118/-DCSupplemental>.

Published February 2, 2021.

nature and the actomyosin-mediated cell contractility (17, 28–32). Adhesion enhancement at the cell–cell contact is more complex in terms of timescale. Load-induced cell–cell adhesion strengthening has been shown via the increase in the number of adhesion complexes (33–35) or by the clustering of adhesion complexes (36–39), which occurs on a timescale ranging from a few minutes up to a few hours after cells experience an initial load (28). External load on the cell–cell contact also results in a prolonged cell–cell adhesion dissociation time (40, 41), suggesting cadherin bonds may transition to catch bonds under certain loading conditions (42, 43), which can occur within seconds (44). With the increase in cellular tension, failure to dissipate the stress within the cell layer at a rate faster than the accumulation rate will inevitably lead to the fracture of the cell layer (45). Indeed, epithelial fracture often aggravates the pathological outcomes in several diseases, such as acute lung injuries (46), skin disorders (47), and development defects (48). It is generally accepted that stress accumulation in the cytoskeleton network (49, 50) and potentially in the cytoplasm is strain-rate-dependent (51). However, to date, there is a lack of understanding about the rate-dependent behavior of cell–cell adhesions, particularly about which of the stress-relaxation mechanisms are at play across the spectrum of strain rates. In addition, it remains unclear how the stress relaxation interplays with adhesion enhancement under large strains, especially at high strain rates which may lead to fracture, that is, a complete separation of mature cell–cell adhesions under a tensile load (45, 52, 53). Yet, currently, there is a lack of quantitative technology that enables the investigation of these mechanobiological processes in a precisely controlled manner. This is especially true at high strain rates.

To delineate this mechanical behavior, the cleanest characterization method is to directly measure stress dynamics at a single mature cell–cell adhesion interface. Specifically, just as a monolayer cell sheet is a reduction from three-dimensional (3D) tissue, a single cell–cell adhesion interface, as a reduction from a monolayer system, represents the smallest unit to study the rheological behavior of cellular junctions. The mechanistic understanding uncovered with this single unit will inform cellular adaptations to a more complex stress microenvironment *in vivo* and *in vitro*, in healthy and diseased conditions. To this end, we developed a single-cell adhesion micro tensile tester (SCA μ TT) platform based on nanofabricated polymeric structures using two-photon polymerization (TPP). This platform allows *in situ* investigation of stress–strain characteristics of a mature cell–cell junction through defined strains and strain rates. With SCA μ TT, we reveal some interesting biophysical phenomena at the single cell–cell junction that were previously not possible to observe using existing techniques. We show that cytoskeleton growth can effectively relax intercellular stress between an adherent cell pair in a strain-rate-dependent manner. Along with cadherin-clustering-induced bond strengthening, it prevents failure to occur at low strain rates. At high strain rates, insufficient relaxation leads to stress accumulation, which results in cell–cell junction rupture. We show that a remarkably large strain can be sustained before junction rupture (>200%), even at a strain rate as high as 0.5 s⁻¹. Collectively, the rate-dependent mechanical characterization of the cell–cell junction builds the foundation for an improved mechanistic understanding of junction adaptation to an external load and potentially the spatiotemporal coordination of participating molecules at the cell–cell junction.

Results

SCA μ TT, a Single-Cell Adhesion Interface Mechanical Characterization Platform. A microstructure has been designed and fabricated to interrogate the mechanical behavior of the cell–cell adhesion complex under large strains (Fig. 1A). This structure, fabricated from IP-S photoresist using TPP (54), consists of two movable

islands on top of vertical “A-shaped” beams with well-calibrated stiffness. A pair of epithelial cells are deposited onto the movable islands with one on each side. The formation of a mature cell–cell junction between the cell pair mechanically couples the two islands. To interrogate the mechanical responses of the cell pair, we displace one of the islands (Island 2) using a nanopositioner from an atomic force microscope (AFM) system in a precisely controlled manner, while the other one (Island 1) is consequently displaced by the tensional force transmitted through the cell–substrate adhesion and the cell–cell junction. The coupling between the nanopositioner and Island 2 is facilitated by capturing the pillar structure on Island 2 using an engineered AFM probe in which a through-hole is drilled by focused ion beam (FIB) etching. The device is integrated on top of an inverted microscope for monitoring the displacement of the islands, from which the deformation of the supporting beams is determined based on digital image correlation (DIC). Island 1, therefore, functions as a force sensor that can be used to measure nano-Newton range forces by relating its displacement to the spring constant of the beam that supports it (Fig. 1B). A detailed illustration of the platform is shown in *SI Appendix*, Fig. S1.

Design, Fabrication, and Mechanical Characterization of the Sensing Structures. The stiffness of the supporting beams was designed to be as close to the stiffness of the cell–cell junction (0.01 N/m to 0.5 N/m) (55) as possible to acquire the best balance between force-sensing resolution and applied strain to the cell–cell junction, with the ability to measure a force in the range of 0 to 50 nN at the junction (56, 57). Compared with horizontal beams, vertical beams offer greater control of their length, which allows for easy adaptation to this desired stiffness and offers better structural stability during the TPP fabrication process (*SI Appendix*, section 2 and Figs. S2 and S3). A set of vertical “A-shaped” beams were designed and fabricated considering different constraints in beam stiffness, beam stability, fabrication limitations, and imaging requirements (*SI Appendix*, section 2). To confine the migration of the deposited cells, a bowtie structure was designed and fabricated with one trapezoid on each island. The area of the trapezoid and the length of its opening edge were optimized to preserve the physiological conditions with an area large enough to sustain cell growth and an opening edge of 12 μ m to facilitate junction formation at the interface between the two islands (56, 57) (Fig. 1C). The gap between the two movable islands, particularly between the bowtie opening where the junction forms, should be kept to a minimum to facilitate junction formation, but a gap distance of less than 2 μ m leads to unwanted polymerization of the resin that tethers the two islands during the fabrication process. We increased the gap of the nonbowtie region to 6 μ m to reduce the risk of attachment of the islands (Fig. 1D).

To measure the stiffness of the “A-shaped” beam structure, a tipless cantilever probe with a thermally tuned stiffness was used to apply force on an isolated sensing structure in phosphate-buffered saline (PBS) solution. Based on the displacement of the probe and the force measurement from the AFM probe, the deflection and subsequently the stiffness of the microstructure were determined (Fig. 1E and *SI Appendix*, section 3). For each measurement, the automated detection of the AFM was used to initiate contact between the probe and the structure. Once contact was established, a constant probe displacement rate was initiated to apply force on the structure until the force set point was achieved. The probe was then retracted until it was no longer in contact with the structure before beginning the process again. This produced the force–displacement curve, from which the stiffness of the beam can be extracted (Fig. 1F). The calculated beam stiffness was found to be 0.049 \pm 0.005 N/m under liquid conditions (Fig. 1G), which is within the desired range. This

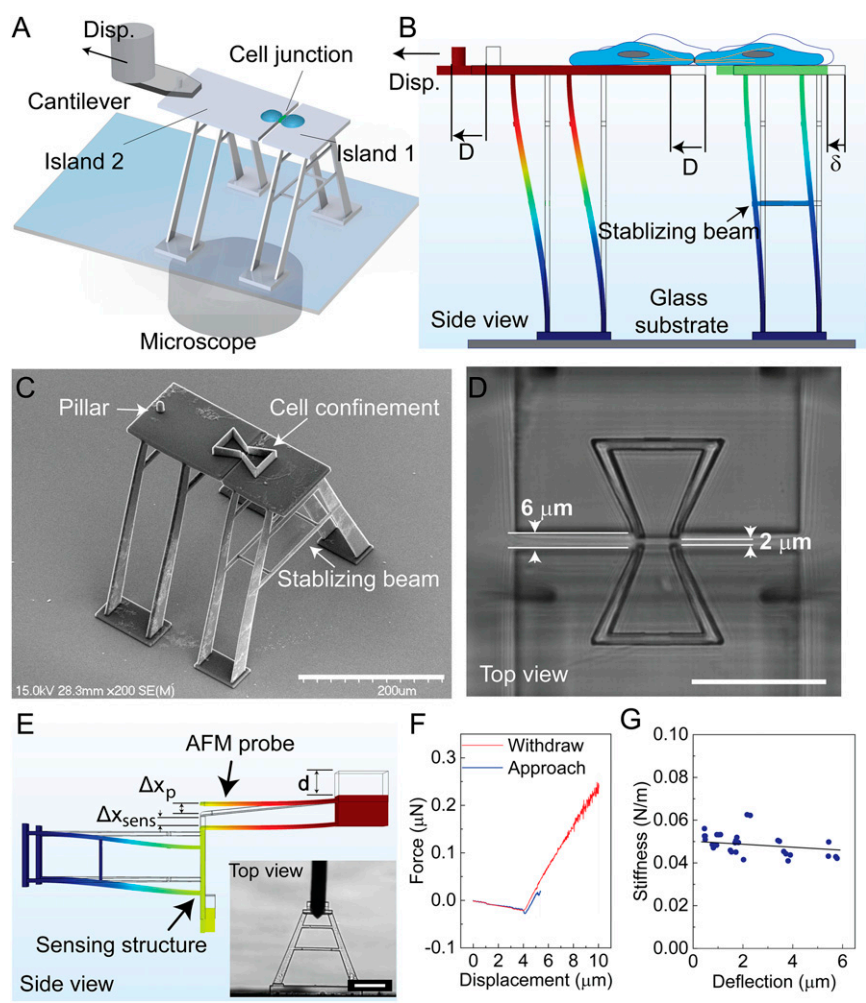


Fig. 1. A single cell–cell adhesion interface mechanical characterization platform. (A) A single cell pair with junctional contacts is formed on Islands 1 and 2. To apply mechanical strain to the cell–cell junction, an AFM-based manipulation system displaces Island 2. (B) The deflection of Island 1 (δ) under the applied displacement (D) is recorded to determine the force–displacement relationship. (C) Scanning electron microscopy (SEM) image of the structures fabricated on top of a glass substrate. The bowtie structures confine the cells on each island. (D) The two islands were spaced $6\ \mu\text{m}$ apart to prevent attachment of the islands to each other, with a $2\text{-}\mu\text{m}$ gap between the cell-confining bowties to allow formation of the cell–cell junction. (E) To measure the stiffness, an AFM probe applies force to the structure until a displacement set point is achieved, and then retracts. The AFM records the applied force, P_{AFM} , and vertical displacement d . The vertical structure displacement, Δx_{sens} , and deflection of the AFM probe, Δx_p , are determined from the AFM output. The inset image shows the probe applying force onto the structure. (F) A representative force–displacement curve obtained at a maximum applied force of $294\ \text{nN}$ is shown. (G) Sensing structure stiffness, k_{sens} , versus structure deflection, Δx_{sens} is plotted ($n = 30$). (Scale bars, $200\ \mu\text{m}$ in C; $50\ \mu\text{m}$ in D; $100\ \mu\text{m}$ in E.)

stiffness value remains valid for a sensing beam deflection of $\sim 6\ \mu\text{m}$ (i.e., a maximum force of $294\ \text{nN}$), displaying a large linear range. It is worth mentioning that the TPP printing parameters, including laser power and scan speed, can have a significant influence on the measured stiffness. Considering the resolution of DIC at a few tens of nanometers, this sensing beam stiffness can resolve the forces of a few cadherin bonds [$\sim 40\ \text{pN}$ for each cadherin bond (58)]. Furthermore, the elastic behavior of the sensing beam is confirmed with a stretch-and-release experiment showing negligible plastic deformation (SI Appendix, section 4 and Fig. S4).

Formation of Cell–Cell Adhesion Junctions on the Platform. Cells were deposited into the bowtie structure using an Eppendorf single-cell isolation setup, which includes a pressure controller, a 3D manipulator, and microcapillary (59) (SI Appendix, section 5 and Fig. S5). To enhance cell attachment to the structure, fibronectin was used to coat the surface of the bowtie structure. As shown in Fig. 2A, a pair of A431 cells were successfully deposited

and placed inside the bowtie structure. The cells expressed green fluorescent protein (GFP)-tagged E-cadherin (E-Cad) and were stained for F-actin and nucleus after being deposited and incubated for 16 h. A mature cell–cell junction, defined as the homeostatic state when E-Cad levels and distribution are stabilized at the cell–cell contact (60), is formed between the cell pair as indicated by the expression of GFP-tagged E-Cad, which bridges the gap between the two islands and mechanically couples them (Fig. 2B and C). The immunofluorescence images of these cells on the structure suggest that the polymer material used in the TPP fabrication is biocompatible and allows for proper cell attachment and growth. Staining zyxin, a widely used mature focal adhesion protein marker (61), together with F-actin confirms that cells successfully form focal adhesions on the structure (Fig. 2D). To find the best time for mechanical characterization after cell deposition, a time-lapse study was performed (4, 8, 16, and 24 h). The results showed that cells do not form a mature junction before 16 h. However, they start proliferating after 24 h, resulting in more than two cells within each bowtie confinement

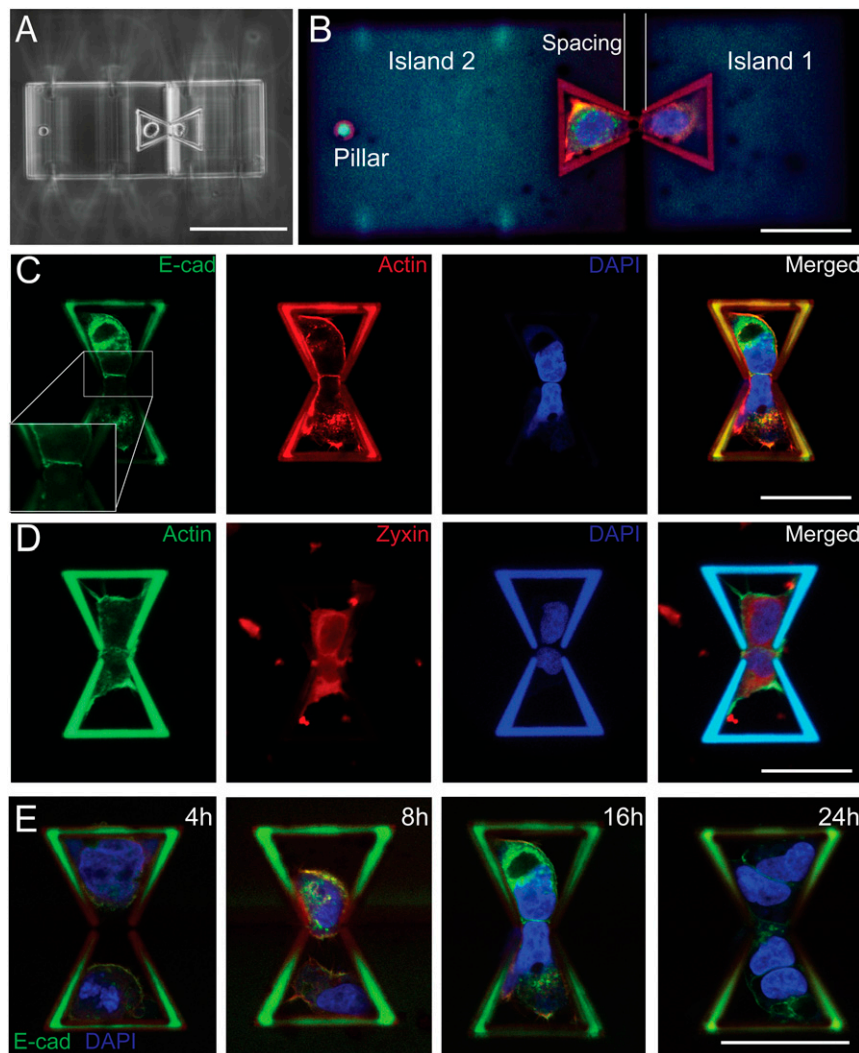


Fig. 2. Cell–cell adhesion formation and cell growth on the scaffolds. (A) Phase-contrast image shows a pair of suspended A431 cells deposited onto the fabricated structure in the opposing bowtie confinement scaffolds. (B) The deposited cell pairs adhered onto the scaffold and started to form a cell–cell junction at the gap to couple the two movable islands. Cells expressing GFP-tagged E-Cad were stained for actin (red) and the nucleus (blue). (C) A431 cells expressing GFP-tagged E-Cad were imaged 16 h after deposition with actin (red) and nucleus (blue) staining. (D) Zyxin (red), actin (green), and nucleus (blue) were stained to visualize the formation of focal adhesion 16 h after deposition. (E) Time-lapse images show the junction formation process, with cells expressing E-Cad GFP stained for nucleus (blue) at 4, 8, 16, and 24 h. (Scale bars, 100 μm in A; 50 μm in B to E.)

(Fig. 2E). Therefore, prior to mechanical testing, cells were incubated for 16 h after cell deposition.

Displacement-Controlled Mechanical Characterization of the Cell–Cell Junction. To interrogate the mechanical behavior of the cell–cell junction, we stretched the junction by displacing Island 2 at different rates. We examined four strain rates ranging from 0.005 s^{-1} to 0.5 s^{-1} and observed different modes of stress relaxation and cell–cell adhesion failure that are strongly strain-rate–dependent. We first stretched the cell pair at a strain rate of about 0.005 s^{-1} (100 nm/s in displacement rate) and observed that none of the junctions failed at the end of the 50 μm displacement. A typical set of time-series images shows that there is no sign of rupture in the cell–cell junction (Fig. 3A). The stress–strain curve exhibits a typical viscoelastic behavior wherein the stress increases nonlinearly with a decreasing rate as the strain increases, and the cell pairs are elongated to a maximum strain of $221.8 \pm 8.2\%$ at a maximum stress of $1.72 \pm 0.73\text{ kPa}$ (Fig. 3B). Under a strain rate of 0.05 s^{-1} , cell–cell

junctions begin to show some signs of rupture through a gradual necking process seen in the time-series images and experience a maximum strain of $217.8 \pm 10.0\%$ and stress of $1.09 \pm 0.63\text{ kPa}$ at the point of failure (Fig. 3C and D). The stress–strain curve shows three different regions: a viscoelastic region, a plateau region (i.e., necking process), and a linear region up to failure at 217.8% strain. Among all the stretch tests performed under this strain rate ($n > 20$), 47% of them resulted in complete cell–cell adhesion rupture, indicating that 0.05 s^{-1} may represent a critical strain rate beyond which stress accumulation induced by mechanical stretching outperforms stress relaxation. Similar observations can be made from a strain rate of 0.25 s^{-1} with a less obvious plateau region, a higher stress level at failure, and more rapid and complete junction failure (Fig. 3E and F). All stretch tests at the strain rate of 0.25 s^{-1} resulted in complete junction rupture, in clear contrast to the 0.05 s^{-1} strain rate. At a strain rate of 0.50 s^{-1} , the stress–strain curve starts with a viscoelastic region, followed by a linear region up to the rupture point. A stress level of $3.04 \pm 1.36\text{ kPa}$ was observed at the failure point and junctions failed at $215.1 \pm 37.4\%$ strain (Fig. 3G and H).

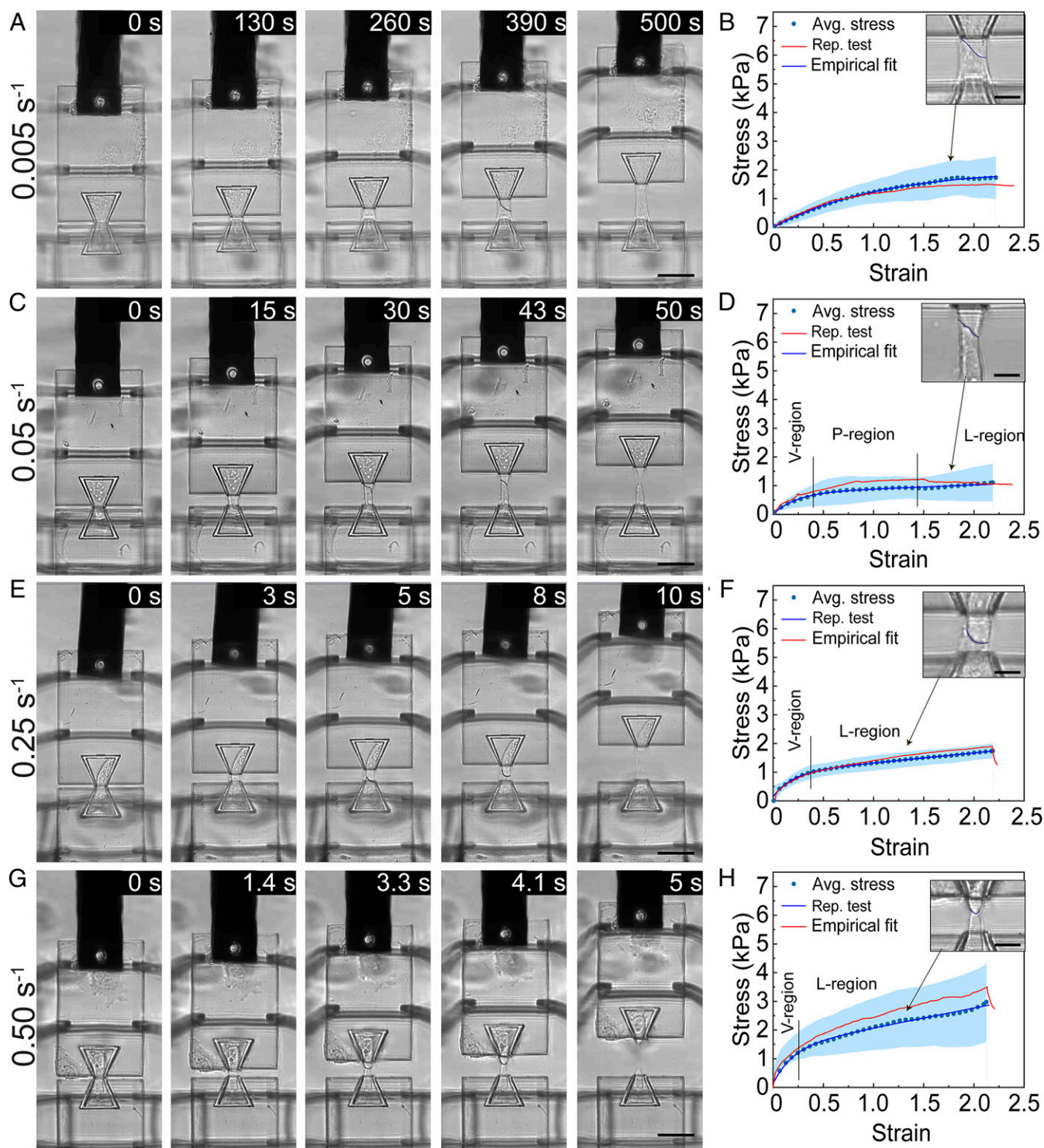


Fig. 3. Displacement-controlled mechanical characterization of a single cell-cell junction at different strain rates. Representative image frames and the corresponding stress-strain curves are shown for stretch tests performed at strain rates of 0.005 s^{-1} (A, B), 0.05 s^{-1} (C, D), 0.25 s^{-1} (E, F), and 0.50 s^{-1} (G, H). For each strain rate tested, Island 2 was displaced by $50\text{ }\mu\text{m}$. For B, D, F, and H, an average stress-strain curve (Avg. stress, dotted line) \pm SD (blue region), a representative stress-strain curve (Rep. stress, red curve), and an empirical fit for the average stress (Empirical fit, blue curve) are shown. The insets for B, D, F, and H show the zoom-in images of the cell-cell junctions at the strains indicated by the arrows. In D, F, and H, the regions are marked with viscoelastic region (V-region), plateau region (P-region), and linear region (L-region). The average stress-strain curves in B, D, F, and H represent data from 11, 12, 7, and 7 stretch tests, respectively. (Scale bars, $50\text{ }\mu\text{m}$ in A, C, E, and G; $15\text{ }\mu\text{m}$ in the inset of B, D, F, and H.)

The gradual disappearance of the plateau region from low strain rate to high strain rate tests suggests stress accumulation at high strain rate due to lagging and inadequate stress relaxation.

Our tensile tests demonstrate that the cell pair can withstand a remarkably large strain level before the cell-cell junction completely ruptures. This clearly contrasts with data obtained from

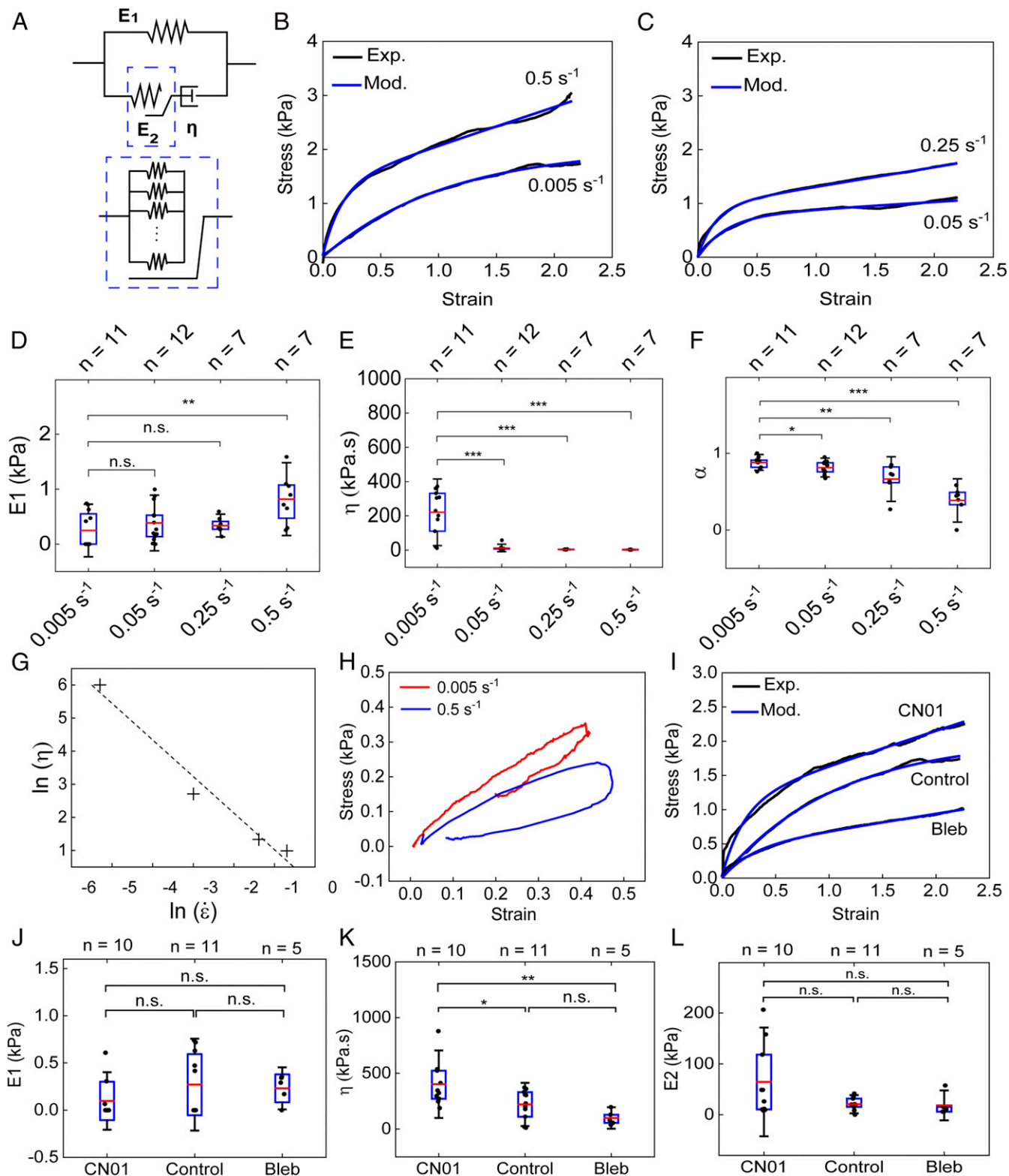


Fig. 4. Strain-rate-dependent and actomyosin-contraction-controlled viscoelastic behavior of the cell pair. (A) Diagram of the modified standard linear solid (MSLS) model that was used for fitting the experimental data. (B, C) The stress-strain curves obtained by applying stretch at different strain rates (0.005 s⁻¹, 0.5 s⁻¹, 0.25 s⁻¹, and 0.50 s⁻¹) were fitted using Eq. 4 according to the MSLS model. (D–F) Box plots comparing the values of E_1 (D), η (E), and α (F) obtained from fitting the stress-strain curves using Eq. 4 for different strain rates. (G) The predicted viscosity is plotted with respect to the strain rates in a log-log scale. (H) Hysteresis analysis is shown by recording the stress-strain relationship following a full cycle of application and release of tensile load on a cell pair at two strain rates (0.005 s⁻¹ and 0.50 s⁻¹). (I) The stress-strain curves obtained by stretching cells treated with CN01, Bleb, and DMSO control at a rate of 0.005 s⁻¹ are fitted using Eq. 4. (J–L) Box plots comparing the values of E_1 (J), η (K), and E_2 (L) obtained from fitting the stress-strain curves for cells treated with CN01 and Bleb using Eq. 4. For each box plot, the number of experiments is indicated on top of each graph. * $P < 0.05$, ** $P < 0.01$, *** $P < 0.001$.

suspended cell doublets without a mature cell–cell adhesion using dual micropipette aspiration (DPA), in which cadherin bonds rupture at small strain and low levels of stress (62). Under low strain rates, the cell–cell junction remains largely intact even when the strain is higher than 200%. Comparing with the 0.50 s^{-1} strain rate, the lower maximum stress under the strain rate of 0.005 s^{-1} , at which cell–cell adhesion complexes remain largely intact, indicates the existence of another effective stress dissipation scheme inside cells. Considering the dynamic nature of cytoskeletons among all the intracellular structures, we speculate that the mechanical stress is dissipated via the remodeling and reorganization of their cytoskeletons. However, under high strain rates, the cell pair dissipates stress primarily through the dissociation of cell–cell adhesion complexes, and complete breakage occurs at a strain level of $\sim 200\%$. In addition, all failures occur at the cell–cell contact symmetrically through the rupture of the cell–cell adhesion complex, as observed from stretching tests at different strain rates (*SI Appendix, Fig. S6 and Movies S1–S4*). The image series of the tensile test (Fig. 3 *A, C, E, and G*) and the zoom-in images of the cell–cell adhesion region (*Inset of Fig. 3 B, D, F, and H*) show the decrease in length of the mutual cell junction until complete separation, suggesting intermediate bond dissociation accompanying the straining process, which leads to ultimate cell adhesion complex failure. The absence of asymmetrical failure, potentially at the cytoskeleton to cell membrane tether at one side of the cell pair, implies that the cell–cell adhesion complex represents the weakest link in the cytoskeleton–cell adhesion–cytoskeleton system. Moreover, the rupture of the cell–cell junction occurs in a gradual fashion at lower strain rates, like unzipping a zipper, with localized snap and retraction of the cytoskeleton near the failure point at the edge of the cell–cell contact.

A Mechanosensing Constitutive Model for the Viscoelastic Behavior of a Cell Pair. The stress–strain relationships from the four types of tensile tests of varied strain rates can be well fitted with an empirical exponential growth function plus a linear function: $\sigma = -Ae^{-B\varepsilon} + C\varepsilon$, supporting an overall viscoelastic behavior (Fig. 3 *B, D, F, and H*). Considering that the cell membrane deforms along with their intracellular components when a pair of cells are stretched, the standard linear solid (SLS) model (*SI Appendix, Fig. S7A*), consisting of a Maxwell branch and an elastic branch, is the simplest model that can effectively capture such a viscoelastic behavior. The SLS model has been widely used to model the mechanical responses of suspended cells, where the Maxwell branch represents the intracellular components while the elastic branch represents the plasma membrane (63). Since minimal deformation of the cell nuclei was observed even at a strain level as large as 200% in our tensile tests, we expect that the elastic element in the Maxwell branch is primarily contributed by the cytoskeleton. Although the SLS model can reproduce the general shape of the stress–strain relationships, it predicts that the elastic modulus of the spring in the Maxwell branch increases with the increase in the strain rate (*SI Appendix, Fig. S7B*). This prediction is in contradiction to the fact that cytoskeleton growth hardly occurs at high strain rates given the limited response time. Alternatively, we modified the SLS model by incorporating a mechanosensing component to account for the stress dissipation mediated by cytoskeleton remodeling (17, 64). As shown in Fig. 4A, the spring with Young’s modulus of E_1 represents the cell membrane, while the second spring with Young’s modulus of E_2 and the dashpot with the viscosity of η represent the elastic and viscous elements of intracellular components, respectively. The viscous component is contributed by the combined effect of cytoplasmic and cytoskeleton friction (51). The cytoskeleton of adherent cells constantly undergoes reorganization through dynamic assembly and disassembly to

maintain its mechanical homeostasis in response to the tensile load. We expect that the elastic element of intracellular components is primarily contributed by the cytoskeleton, and E_2 can be considered as the collective moduli of all stress fibers that sustain the load and should be proportional to the number of individual stress fibers within the plane perpendicular to the stretching direction, as demonstrated by the inset in Fig. 4A. The value of E_2 should be collectively determined by the cell–cell junction length and cell–cell adhesion complex density. The continuous growth of the cytoskeleton is expected to lead to an increase in the resting length of the second spring, which could partially or even completely relax the passive stress (σ_{S2}) resulting from stretching:

$$\sigma_{S2} = E_2(\varepsilon_{S2} - \varepsilon_0), \quad [1]$$

where ε_{S2} and ε_0 are the total strain of the second spring and the strain resulting from the continuous growth of the cytoskeleton, respectively. We relate the cytoskeleton growth rate with the strain rate of the second spring through a model parameter α :

$$\dot{\varepsilon}_0 = \alpha \dot{\varepsilon}_{S2}, \quad [2]$$

where $0 \leq \alpha \leq 1$. When $\alpha = 0$, $\dot{\varepsilon}_0 = 0$, suggesting that the cytoskeleton does not grow at all, which corresponds to stretch with a very high strain rate. When $\alpha = 1$, Eq. 2 reduces to $\dot{\varepsilon}_0 = \dot{\varepsilon}_{S2}$, indicating that the growth of the cytoskeleton is able to completely release the passive stress, which could occur under stretch with an extremely low strain rate. Therefore, α can be considered as an effective parameter to indicate the growth level of the cytoskeleton during the stretch test and thus the stress dissipation efficiency. The model predicts the following time-dependent relationship between stress (σ_{tot}) and strain (ε_{tot}):

$$\dot{\sigma}_{tot} + \frac{(1-\alpha)E_2}{\eta}\sigma_{tot} = [E_1 + (1-\alpha)E_2]\dot{\varepsilon}_{tot} + \frac{(1-\alpha)E_1E_2}{\eta}\varepsilon_{tot}. \quad [3]$$

Under a constant strain-rate condition, Eq. 3 yields

$$\sigma_{tot} = E_1\varepsilon_{tot} + \eta\dot{\varepsilon}_{tot} \left[1 - \exp\left(-\frac{(1-\alpha)E_2}{\eta}\frac{\varepsilon_{tot}}{\dot{\varepsilon}_{tot}}\right) \right]. \quad [4]$$

As shown in Fig. 4B and C, Eq. 4 is able to robustly capture the viscoelastic responses of cells under different strain rates. Fitting the stress–strain curves obtained in our stretch tests with Eq. 4 allows us to predict how E_1 , $(1-\alpha)E_2$, and η vary with the strain rate.

Our model predicts that E_1 is independent of the strain rate and has an average value of $\sim 1.2 \text{ kPa}$ (Fig. 4D), which is consistent with previously reported values (51, 65). The viscosity η is predicted to monotonically decrease with the strain rate (Fig. 4E), suggesting that the cytoplasm is a shear-thinning material. Such a shear-thinning feature has been identified for the cytoplasm of several other types of cells previously (66, 67). Plotting the predicted viscosity against the strain rate in a logarithmic scale reveals that the mechanical behavior of the cytoplasm can be approximated as a power-law fluid following the Oswald equation, that is, $\eta = K\dot{\varepsilon}^{(n-1)}$, with the exponent of $n = -0.104$ (Fig. 4G). In general, shear thinning is caused by flow-facilitated disentanglement of polymer chains, which is consistent with the expected enhanced alignment of cytoskeleton structures after cells are subjected to uniaxial stretching (68). Since the cells are expected to have similar cytoskeleton structures to start with, we can directly compare the stress dissipation efficiency mediated by the cytoskeleton growth by assuming that E_2 has the same value. The predicted decrease in α from low strain rate to high strain rate suggests that the stress dissipation

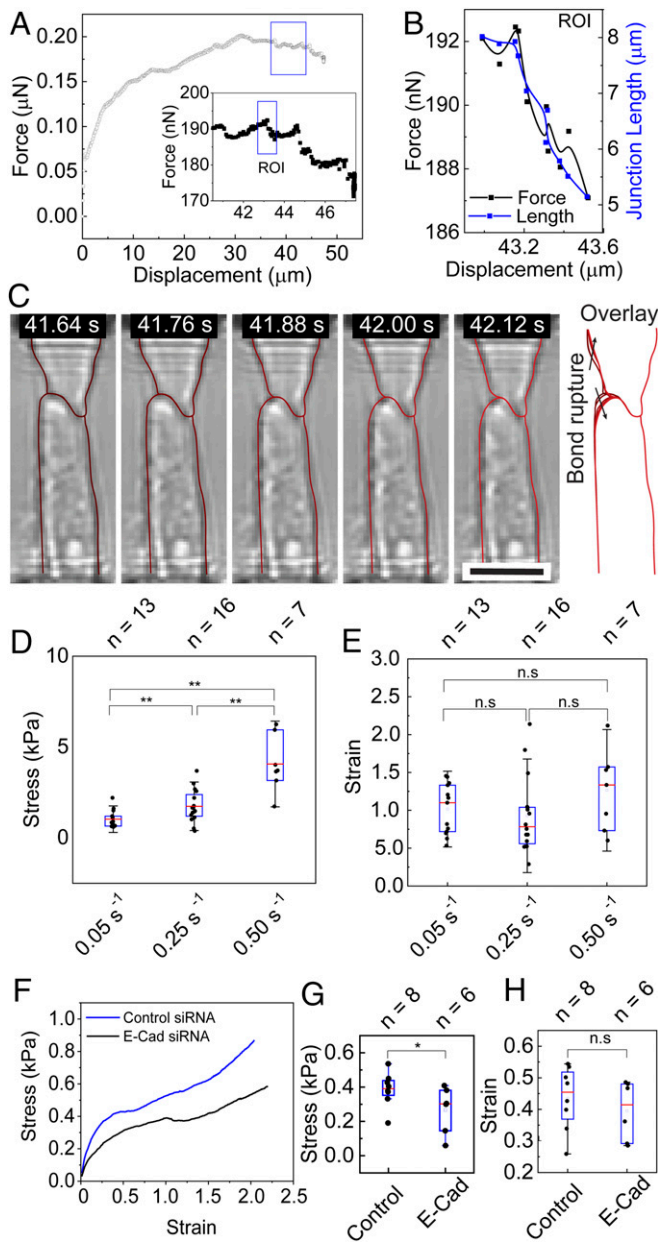


Fig. 5. Cadherin bond rupture exhibits rate-dependent behavior during strain-rate-controlled stretch. (A) A representative force–displacement curve obtained at a strain rate of 0.05 s^{-1} is shown. Inset shows the zoom-in of the portions of the force–displacement curve indicated in the box. (B, C) The force–displacement curve (black curve) and junction length (blue curve) (B) within the ROI in the inset of (A) are shown, with the outline of each cell traced in corresponding frames (C). The overlay in (C) shows the change in cell–cell junction length and shape of each cell (dark red in the first frame and light red in the last frame). (D, E) Stress levels (D) and strain levels (E) at which the initiation of bond rupturing occurs for the tensile tests at different strain rates: 0.05 s^{-1} ($n = 13$), 0.25 s^{-1} ($n = 16$), and 0.50 s^{-1} ($n = 7$). (F–H) Average stress–strain curves (F), as well as stress levels (G) and strain levels (H) at which the initiation of bond rupturing occurs, for tensile tests at 0.05 s^{-1} on cells with E-Cad siRNA knockdown ($n = 6$) and control siRNA ($n = 8$). * $P < 0.05$. (Scale bars, $25\text{ }\mu\text{m}$ in C, Inset.)

efficiency decreases with strain rate as a result of reduced cytoskeleton growth (Fig. 4F). The predicted rate-dependent growth of the cytoskeleton is supported by the clear difference in the residual plastic strain after releasing the tensile load in our hysteresis tests (Fig. 4H). We stretched the cell pair under two

different strain rates (0.005 s^{-1} and 0.50 s^{-1}) to a strain level of about 40% and then completely released the mechanical load. The cell pair stretched under the strain rate of 0.005 s^{-1} resulted in a plastic strain of $\sim 20\%$. However, less than 10% plastic strain is observed for the cell pair stretched under the strain rate of 0.50 s^{-1} , suggesting limited cytoskeleton growth under the high strain rate.

We next subjected the cell pair to cellular contractility modulators, RhoA Activator I CN01 and myosin II inhibitor blebbistatin (Bleb), to examine the impact of actomyosin activity on the mechanical behavior of the cell pair under mechanical stress. Stress–strain curves collected at a strain rate of 0.005 s^{-1} show a clear contrast between samples treated with CN01, Bleb, and dimethyl sulfoxide (DMSO) control (SI Appendix, section 8 and Fig. S8). Specifically, CN01 raises the overall stress level compared with controls at the same strain, while Bleb reduces the stress accumulation (Fig. 4J). The stress–strain curves were then analyzed using the constitutive model. As expected, E_1 stays the same for all conditions (Fig. 4J). Enhancement of actomyosin contractility by CN01 significantly increases η and E_2 , while Bleb reduces both of them (Fig. 4K and L). The increase (decrease) in both η and E_2 by CN01 (Bleb) is consistent with the enhanced (reduced) stress fiber formation. It is worth mentioning that the stress increase induced by CN01 can be partially suppressed by subsequent addition of ROCK inhibitor, exhibiting a reverse effect on the contractility modulation, which can be captured dynamically by our SCA_{TT} platform (SI Appendix, Fig. S9). Collectively, our data support the idea that stress dissipation is facilitated by the actin filament growth during tensile loading conditions.

Cadherin Strengthening and Rupture under Rate-Dependent Stretch of Cell–Cell Junction. We attribute the observed necking process to the rupture of cell–cell adhesion bonds, which is most apparent under the intermediate strain rate. A few cadherin bonds are ruptured in discrete steps at the edge of the cell–cell junction, which corresponds to a small drop in the measured forces in the force–displacement curve (Fig. 5). To investigate the bond rupture, we selected a representative example of the stretch tests at the strain rate of 0.05 s^{-1} with obvious regions of junction rupture followed by stiffening, which is represented by each drop and rise in the curve (Fig. 5A). The rupture of bonds releases the force in the stress fibers that were in direct connection with the bonds and locally relaxes the stretched cell membrane, consequently leading to a drop of the measured force. One representative region of interest (ROI) is plotted in Fig. 5B, in which a total force drop of 5 nN and a junction length reduction of $\sim 3\text{ }\mu\text{m}$ were observed for an $\sim 490\text{-nm}$ displacement (SI Appendix, section 10 and Fig. S10). Correspondingly, a total of 10 image frames were captured showing the snap and retraction of the cytoskeleton at the edge of the cell–cell junction (Fig. 5C), and each discrete snap motion corresponds to a small drop in force. Considering the strength of a single cadherin bond of around 40 pN (69), this decline is the result of rupturing about a few hundred cadherin bonds in each discrete event with a resolution of a few bonds.

The bond dissociation events also exhibit strong strain-rate dependency. First, at a very low strain rate, the absence of bond rupture may be attributed to cadherin strengthening. This is confirmed by the clustering of GFP-tagged E-Cad when the cell doublet is subject to low levels of strain ($<100\%$) at the strain rate of 0.05 s^{-1} (SI Appendix, Fig. S11). It has been observed that cadherin bond clustering in epithelial cells under tensile load occurs in a timescale of minutes, right in line with the time span of a low strain rate tensile test (about 10 min) (33). Second, the critical stress level at which cadherin bonds show initial signs of dissociation increases significantly with increasing

strain rate (Fig. 5D). As shown in Fig. 5E, the initiation of bond rupture events occurs at similar strain levels of around 100% for all three strain rates. However, the critical stress is significantly higher for 0.50 s^{-1} (4.04 kPa) compared with 0.5 s^{-1} and 0.25 s^{-1} (0.99 kPa and 1.72 kPa, respectively). Considering the time span of a few seconds for a tensile test at the strain rate of 0.50 s^{-1} , bond clustering may not be the main contributor to the observed increase in the critical stress. On the other hand, the observed increase in the strength of cadherin bonds agrees well with previous reports from single-molecule force microscopy studies of E-Cad bonds, which showed that the peak rupture force in E-Cad bonds increases logarithmically with the loading rate (69, 70). Knockdown of E-Cad by small interfering RNA (siRNA) resulted in a decrease in the overall stress level during the strain application (Fig. 5F). Analysis of the stress-strain curves of E-Cad knockdown cell pairs showed a significant decrease in the critical stress, as compared with controls using control siRNA (*SI Appendix, section 12 and Fig. S12 and Fig. 5G*). Interestingly, the strain levels at which cadherin bonds initiate unbinding remain unchanged with E-Cad knockdown (Fig. 5H). This may suggest that the reduction in the number of E-Cad bonds decreased the total tension within the cytoskeleton network and thus the stress level during stretching, while the remaining bonds still rupture at similar strain levels. Collectively, our results demonstrate that E-Cad adhesions regulate the load-bearing potential of the cell-cell junction under tensile load and play a major role in the rate-dependent strengthening of the cell-cell junction.

Discussion

In this study, we fabricated a polymeric microstructure using TPP for displacement application and force sensing to examine the rate-dependent mechanical behavior of a single cell-cell adhesion complex. To faithfully characterize the intricacy of the biophysical and biochemical response of an individual cell-cell adhesion interface under large strains, a functional technique needs to fulfill the following requirements. First, it should have a highly sensitive force-sensing component that allows easy quantification of pico- or nano-Newton forces. Second, it should have the capability to apply mechanical strain or stress in a controlled manner. Third, the testing can be conducted under physiologically relevant conditions, especially allowing the formation of mature cell-cell junctions and cell-extracellular matrix (ECM) adhesions. Although several techniques have been developed for the quantitative assessment of cell-generated forces, including traction force microscopy (TFM) (71), elastomer-based micropillar arrays (57), and 3D-printed microscaffolds (72, 73), they are restricted to static observations and unable to apply mechanical stimuli, not to mention strain-rate-controlled mechanical stretch. Techniques do exist to apply mechanical strain to a monolayer of cells, but the stress within individual cell-cell adhesions cannot be determined (52). Further, when a defined load is applied to individual cell-cell junctions in studies using AFM-based single-cell force spectroscopy (SCFS) (58, 74) and DPA (75, 76), it can only be carried out on isolated suspended cells in which mature intercellular junctions are yet to form, and the focus can only be placed on the separation of cadherin bonds while the effect of stress relaxation of the cytoskeleton and the cell-ECM interactions are inaccessible (62).

SCA μ TT is a platform that allows in situ interrogation of the stress-strain characteristics of a mature cell-cell junction through defined strain and strain rate, promoting a paradigm shift in the mechanical characterization of cell-cell adhesions. Besides the capabilities discussed above, the throughput for mature cell-cell junction interrogation is also increased due to parallel sample preparation and testing, as the equipment for manipulating or stretching cells does not need to be used to hold cells in place during junction maturation. The presence of the mature cell-ECM junction allows for the application of large

strains as in DPA, whereas the force sensitivity of the beams achieves force and displacement resolution comparable to SCFS (10 pN and 50 nm, respectively) (77). Besides its application in the mechanical characterization of single cell-cell junctions, SCA μ TT can also be used to investigate the cytoskeleton mechanics and dynamics under controlled strains and/or strain rates, as well as in the study of the crosstalk between cell-cell adhesion and cell-ECM adhesion, by incorporating micropillar array-based TFM into our platform. These studies can be carried out not only on cell doublets but also on single cells and cell monolayers with minimal modification to the bowtie structure.

The ability of SCA μ TT to quantify precisely the stress within a cell doublet at different strains enables us to decipher the strain-rate-dependent behavior of the cytoskeleton-junction system as part of the adaptive viscoelasticity of epithelial cell-cell junctions (78). The stress-strain relationship at different strain rates reveals multiple rate-dependent stress dissipation mechanisms orchestrated by the cytoskeleton and the cell-cell junction. We showed that the cytoplasm exhibits a passive shear-thinning viscoelastic behavior following the Oswald equation. This power-law relationship between strain rate and viscosity suggests that such a passive stress dissipation mechanism plays a significant role in the stress response, particularly at high strain rates. It is worth mentioning that this relationship has been identified for the cytoplasm of suspended cells (66, 67) but has never been shown on adherent cells. In addition, we showed that the active cytoskeleton remodeling leads to continuous stress relaxation in the network of the cytoskeleton-cell junction (79). Particularly, loads with a higher strain rate result in limited cytoskeleton growth, and thus, higher stress is accumulated within the network. When stress relaxation from the cytoskeleton growth fails to catch the increased stress induced by the continuous increase of the applied strain, a net accumulation of stress occurs. The increase in stress leads to gradual unbinding of cadherin bonds to relax the stress at low strain rates. A robust junction allows a higher capacity for cytoskeleton tension, while a partially ruptured junction reduces this capacity. Although the expected active cytoskeleton remodeling has not been confirmed directly with high-resolution immunofluorescence imaging due to the strong autofluorescence of the printed microstructures on which cells are grown, it has been validated indirectly by both the hysteresis tests and the contractility modulation experiments using cytoskeleton modulation drugs. Furthermore, as cell-cell adhesion is intimately coupled with cell-substrate adhesion (80), we expect that changing the ECM coating may affect the structure of the cell-cell junction and consequently its mechanical strength. However, we do not expect cell-ECM interaction to fundamentally change its strain-rate-dependent mechanical response.

Directly measuring stress dynamics at a single cell-cell junction captures the real-time fracture process of junction cadherins at high strain rate. Specifically, we showed that epithelial cell-cell adhesions are mechanically the weakest linkage in the junction-cytoskeleton system, and they represent the upper limit for the amount of stress that the system can tolerate before complete junction rupture occurs. However, when the cell-ECM adhesion is not sufficiently strong, failure is more likely to occur at focal adhesions. We observed that cells tended to detach from the islands during stretching experiments when a fibronectin concentration lower than $50 \text{ }\mu\text{g}/\text{mL}$ was used to functionalize the bowtie structure. Moreover, we showed that, at high strain rate, stress accumulation cannot be dissipated fast enough even at low strain levels, and thus, characterization of the critical strain and strain rate at which coordinated stress relaxation and E-Cad clustering can still be sufficient to mitigate stress buildup and to allow for such a remarkable strain tolerance is critical to understand epithelial fracture (45). Further, knockdown of E-Cad changed the strain-rate-dependent behavior of the cell-cell junction, agreeing with previous reports that show E-Cad

regulates epithelial viscoelasticity (81). This may also alter the patterns of cell proliferation and migration, which play important roles in disease outcome. This suggests that the mechanical interrogation platform could be used for quantifying disease states and evaluating the effect of treatments.

Conclusion

In the present work, we developed a mechanical testing platform, SCA μ TT, that can strain the mutual junction of a single cell pair with precisely defined strain and strain rates while simultaneously recording the junction stress. This platform allows in situ mechanical characterizations of a mature cell–cell junction under physiologically relevant conditions and is sensitive enough to resolve bond rupture events with a resolution of a few bonds. With this innovative platform, we performed strain-rate–controlled mechanical characterization of a single mature cell–cell adhesion junction. We showed that cytoskeleton growth of the cell doublet could relax the stress buildup and prevent junction failure at low strain rates. At high strain rates, a synchronized junction failure occurs at remarkably large strain levels. We expect this platform and our biophysical understanding to form the foundation for the rate-dependent mechanics of cell–cell junctions.

Methods

TPP Fabrication. To fabricate the structures shown in Fig. 1 and *SI Appendix, Figs. S2 and S3*, microscale 3D printing based on TPP was used. Computer-aided design (CAD) files in standard tessellation language (STL) format exported from COMSOL 4.2 software were imported into the Describe software (Nanoscribe, GmbH) to compile job files for the Photonic Professional (GT) tool (Nanoscribe, GmbH). The slicing and hatching distances were selected to be 0.4 μ m and 0.3 μ m, respectively. The vendor-supplied liquid photoresist, IP-S, and a 25 \times immersion microscope objective were used to print structures in the galvo-scanning mode using the so-called deep-in laser lithography optical arrangement. Glass coverslips with diameters ranging from 11 to 25 mm and thicknesses of \sim 160 μ m were used as substrates in the present study. Prior to 3D printing, the glass substrates were coated with indium tin oxide (ITO) to achieve optical reflectivity of the IP-S–substrate interface suitable for autofocusing. The ITO layer had a thickness of \sim 50 nm and was deposited using direct current sputtering of an ITO target in an Ar plasma. In our initial tests, we found that the 3D structures printed directly on the ITO-coated glass had insufficient adhesion and would detach from the substrate after prolonged soaking or incubation in aqueous solutions. To address this commonly encountered issue of insufficient adhesion between smooth substrates and 3D structures fabricated using TPP, we used an in-house developed protocol in which an additional layer of porous silicon oxide (PSO) was deposited on top of ITO-coated coverslips. PSO with a thickness of \sim 2 μ m and a high density of nanopores was found to act as an excellent anchoring layer, eliminating detachment of the 3D printed structures from the substrate during soaking and subsequent experiments in aqueous solutions. For all experiments, arrays of structures (varying from 5 \times 4 up to 6 \times 6) were fabricated on each coverslip, allowing for increased throughput in testing.

Cell Culture and Transfection. A431 GFP-tagged E-Cad cells were cultured in a growth medium composed of Dulbecco's modified Eagle's medium and supplemented with 10% fetal bovine serum (Chemie Brunschwig AG) and 1% penicillin-streptomycin (Invitrogen). The experimental medium consisted of CO₂-independent growth medium (Gibco) supplemented with 2 mM L-glutamine (Gibco), 10% fetal bovine serum, and 1% penicillin-streptomycin. All solutions were filtered through 0.22- μ m-pore-size filters before use. Shortly before each experiment, the structure is submerged with 2 mL of the experimental medium. All experiments were performed in a temperature-controlled enclosed chamber at 37 $^{\circ}$ C. Transfection of E-Cad siRNA (SCBT; SC35242) and control siRNA (SCBT; SC37007) were performed using Lipofectamine RNAiMAX Transfection Reagent (Invitrogen), according to the manufacturer's protocol. The expression of GFP was analyzed by fluorescence microscopy after 48 h. Full-length human E-Cad fused at its C terminus to GFP was constructed by first inserting an E-cadherin complementary DNA (cDNA) into pEGFP-N2 (Clontech, Mountain View, CA) and then inserting the tagged construct into a derivative of the LZRS retroviral expression vector. The final cDNA construct was fully sequenced to ensure no errors were introduced during subcloning.

Structure Preparation for Fluorescence Imaging. The structures were placed inside of a glass-bottom Petri dish, washed with 70% ethanol, and immediately soaked with PBS for 10 min until all the ethanol dissolved. The substrate was then submerged in 0.3% volume ratio Sudan Black B (Sigma-Aldrich) in 70% ethanol for 1 h to block the autofluorescence of the polymer. To dissolve excessive Sudan Black, the substrate was submerged in 70% ethanol for 1 h and then soaked with PBS for 10 min. The substrate was then coated with fibronectin to enhance the adhesion and growth of the cells on the structures. Fibronectin solution with a concentration of 50 μ g/mL in PBS was placed on the substrate and left in the incubator for 2 h. Finally, the fibronectin solution was removed, and the substrate was washed with PBS two times.

Structure Preparation for Mechanical Characterization. The structures were placed inside of a glass-bottom Petri dish, washed with 70% ethanol, and immediately soaked with PBS for 10 min until all the ethanol dissolved. The substrate was then coated with fibronectin (50 μ g/mL in PBS) to enhance the adhesion and growth of the cells on the structures. The fibronectin solution was placed on the substrate and left in the incubator for 2 h. The solution was removed, and the substrate was washed with PBS.

Cell Deposition. An Eppendorf single-cell isolation setup was used to pick up and position cells on the stretching structure. This setup had a microcapillary (Piezo Drill Tip ICSI, Eppendorf) with a tip inner diameter of 6 μ m. The microcapillary was connected to a pressure controller (CellTram 4r Air/Oil, Eppendorf), which could control the inside pressure of the pipette. The micropipette position was controlled with a 3D manipulator (TransferMan 4r, Eppendorf) on an inverted microscope. First, the microcapillary was positioned just above a cell on the substrate and brought into contact with the cell membrane. Then, a negative pressure was applied to suck the cell onto the pipette tip. Finally, the cell was retracted from the surface, positioned on the structure, and detached from the pipette tip by applying positive pressure. The same procedure was performed to pick up and position the second cell (*SI Appendix, Fig. S5*).

Immunofluorescence and Microscopy. The A431 cells were E-Cad GFP-tagged to visualize the cell–cell junctions. Alexa Fluor 657 Phalloidin (Invitrogen) was used to stain the actin filaments, and the nuclei were stained with DAPI (Invitrogen). Cells were washed twice with PBS (pH 7.4), fixed using 4% formaldehyde solution in PBS for 15 min at room temperature, and then washed two times with PBS. Subsequently, they were permeabilized with a solution of 0.1% Triton X-100 in PBS for 5 min and then washed twice with PBS. To enhance the quality of the actin fluorescent intensity, 4 drops of Image-iT FX Signal Enhancer (Thermo Fisher) were added and incubated at room temperature with a humid environment for 30 min. After removing the solution and washing with PBS, the phalloidin staining solution with a ratio of 1:100 in PBS was placed on the substrate for 30 min at room temperature and then washed with PBS. Next, the DAPI solution with a ratio of 1:1,000 with PBS was placed on the substrate and incubated for 10 min at room temperature. The solution was removed, and the substrate was washed with PBS. Finally, 3 mL of pure water was added to the Petri dish for imaging. Zyxin staining was performed to visualize the focal adhesion points between cells and the structure. After fixing the cells (see above), the anti-zyxin antibody (Sigma) with a ratio of 1:250 with PBS was added to the sample and refrigerated for 24 h. The solution was then removed, and the sample was washed with PBS. PBS was replaced by goat anti-rabbit IgG (H+L), Superclonal Recombinant Secondary Antibody, Alexa Fluor 647 (Thermo Fisher) and incubated for 1 h at 37 $^{\circ}$ C. Finally, the sample was washed with PBS, and the actin and nuclei staining protocols were performed. Pharmacological treatments modulating cell contractility included 3 μ M Bleb (Sigma-Aldrich) for 2 h and 1 unit/mL Rho Activator I (CN01; Cytoskeleton, Inc., Denver, CO) for 30 min. A Nikon A1-NiE upright confocal system (60 \times water immersion objective) driven by NIS-Elements Confocal image acquisition and analysis program (Nikon software) was used for immunofluorescent imaging of cells on the structures. All image reconstructions and channel alignments were performed within the Nikon software. Zeiss Axio 7 was used for the stretch test. An AFM setup (Nanosurf AG, Switzerland) was installed on the microscope to apply the displacement to the structures.

Cell Lysis, Gel Electrophoresis, and Immunoblotting. A431 GFP-tagged E-Cad cells were lysed with radioimmunoprecipitation assay (RIPA) buffer (50 mM Tris-HCl, pH 7.4, 150 mM NaCl, 5 mM ethylenediamine tetraacetic acid

(EDTA), 2 mM dithiothreitol, 1 mM phenylmethylsulfonyl fluoride (PMSF) and 1% Triton X-100) containing a protease inhibitor mixture (S8830; Sigma). Whole-cell lysates were incubated on ice for 30 min and then centrifuged at $14,000 \times g$ for 20 min at 4 °C. Proteins were separated by sodium dodecyl (lauryl) sulfate-polyacrylamide gel electrophoresis (SDS-PAGE) using 8% gels and blotted onto polyvinylidene fluoride (PVDF) membranes. The blots were incubated overnight at 4 °C with anti-E-Cad (BD Biosciences; 610181), or anti- β -actin (Santa Cruz Biotechnology; SC-47778). Blots were then washed and incubated with horseradish peroxidase (HRP)-conjugated anti-mouse (Jackson immunoresearch), followed by washing and detection of immunoreactivity with enhanced chemiluminescence (Santa Cruz Biotechnology).

Displacement Tracking Using DIC. A modified version of MATLAB DIC was used to analyze the frames from the stretch test. The first frame was considered as the reference, and the rest of the frames were compared to the reference frame to calculate the displacement of each island. An ROI with markers within the region was defined for both islands. Then, the MATLAB code calculated the markers' new coordinates with respect to the first frame, from which the displacement of the islands was calculated. The MATLAB code for calculating the displacement from captured frames is available at <https://github.com/YangLabUNL>.

Stress–Strain Curve Calculation. Each stretch test was recorded and analyzed with a customized DIC-based program to calculate each island's movement. The displacement of each island was obtained by averaging the displacement of markers in the ROI in each frame. Similarly to previous studies on epithelial monolayers (52), the strain was calculated by dividing the difference of the two islands' displacements by the initial length: $\varepsilon = (D - \delta)/L_0$, where D is the Island 2 (actuation) displacement, δ is the Island 1 (sensing) displacement, and L_0 is the initial length. This initial length was defined as the nucleus-to-nucleus distance of the cell pair, which was measured to be $19.18 \pm 0.50 \mu\text{m}$ (SI Appendix, section 13 and Fig. S13). We had assumed that deformation occurred in the region of the cell near to the junction, and the region of the cell behind the nucleus was fully attached to the substrate via cell–ECM adhesion with negligible deformation. This assumption was validated by tracking the movement of marker points inside the nucleus region, and the results showed that, compared with the elongation of the region of the cell near to the junction, the region behind the nucleus remained relatively unmoved (SI Appendix, section 14 and Fig. S14). Understandably, cells adhered to the device via discrete focal adhesion spots at the base of the cell, and these adhesions could actively change during the stretching process. Nevertheless, under large deformation (as the deformation of the cell

pair during the stretch can reach several folds of the initial length), the influence of the small variation of the initial length on the calculated stress–strain relationships can be mitigated. Force was calculated using Hooke's Law, $F = k\delta$, where k is the sensing island stiffness obtained from the AFM experiment. The effective engineering stress was defined by dividing the calculated force by the cross-sectional area of the junctional region, following the same concept adopted by previous studies on epithelial monolayers (52). The cross-sectional area was treated as the junction length multiplied by the thickness of the cell–cell contact region. The measured data showed that the cell–cell junction length varied significantly from one cell pair to another. Thus, the length data obtained from the processing of the cell doublet images in each stretch test were used. The cell–cell contact region was found to be $10.24 \mu\text{m}$ in thickness with limited variations measured from confocal z-stack imaging (SI Appendix, Fig. S13).

Statistical Analysis. Curve fittings were performed in MATLAB. All other data analysis was conducted in Origin. For all box plots, the edges of the box represent SD of the data, and the red line marks the mean of the data. A two-tailed Student's t test was performed for comparison between two data conditions. $P < 0.05$ was considered statistically significant.

Data Availability. All study data are included in the article and/or supporting information. The MATLAB code for calculating the displacement from captured frames is available at <https://github.com/YangLabUNL>.

ACKNOWLEDGMENTS. We acknowledge the funding support from the NSF (Awards 1826135 and 1936065), the NIH National Institutes of General Medical Sciences P20GM113126 (Nebraska Center for Integrated Biomolecular Communication), P20GM104320 (Nebraska Center for the Prevention of Obesity Diseases), P30GM127200 (Nebraska Center for Nanomedicine), 1U54GM115458-01 (Great Plains IDeA-CTR), and R15AR072959. We acknowledge funding support from the Nebraska Collaborative Initiative and EPSCoR FIRST award. Design and fabrication of the TPP structures were conducted at the Center for Nanophase Materials Sciences at Oak Ridge National Laboratory, which is a Department of Energy Office of Science User Facility. C.H. would also like to acknowledge financial support from Nanyang Technological University (Startup Grant M4082352.050) and the Ministry of Education, Singapore, under its Academic Research Fund Tier 1 (M4012229.050). M.D. acknowledges partial support from NIH R01HL154150. We are grateful for the technical assistance of Dr. You Zhou from Center of Biotechnology at University of Nebraska–Lincoln, Dr. Edward Nelson from Nanosurf, and Dr. Benjamin Richter from Nanoscribe.

1. E. Rodriguez-Boulan, I. G. Macara, Organization and execution of the epithelial polarity programme. *Nat. Rev. Mol. Cell Biol.* **15**, 225–242 (2014).
2. T. Kadohama, K. Nishimura, Y. Hoshino, T. Sasajima, B. E. Sumpio, Effects of different types of fluid shear stress on endothelial cell proliferation and survival. *J. Cell. Physiol.* **212**, 244–251 (2007).
3. M. A. Haidekker, C. R. White, J. A. Frangos, Analysis of temporal shear stress gradients during the onset phase of flow over a backward-facing step. *J. Biomech. Eng.* **123**, 455–463 (2001).
4. G. L. Jiang, C. R. White, H. Y. Steven, M. R. Inzunza, J. A. Frangos, Temporal gradients in shear, but not ramp flow, stimulate the proliferation of osteoblast-like cells. *J. Bone Miner. Res.* **16**, S494 (2001).
5. D. Cai *et al.*, Mechanical feedback through E-cadherin promotes direction sensing during collective cell migration. *Cell* **157**, 1146–1159 (2014).
6. L. Zhang, X. Q. Feng, S. F. Li, Review and perspective on soft matter modeling in cellular mechanobiology: Cell contact, adhesion, mechanosensing, and motility. *Acta Mech.* **228**, 4095–4122 (2017).
7. J. S. Park *et al.*, Differential effects of equiaxial and uniaxial strain on mesenchymal stem cells. *Biotechnol. Bioeng.* **88**, 359–368 (2004).
8. M. Chiquet, V. Tunç-Civelek, A. Sarasa-Renedo, Gene regulation by mechanotransduction in fibroblasts. *Appl. Physiol. Nutr. Metab.* **32**, 967–973 (2007).
9. B. M. Gumbiner, Regulation of cadherin-mediated adhesion in morphogenesis. *Nat. Rev. Mol. Cell Biol.* **6**, 622–634 (2005).
10. C. M. Niessen, D. Leckband, A. S. Yap, Tissue organization by cadherin adhesion molecules: Dynamic molecular and cellular mechanisms of morphogenetic regulation. *Physiol. Rev.* **91**, 691–731 (2011).
11. U. Tepass, K. Truong, D. Godt, M. Ikura, M. Peifer, Cadherins in embryonic and neural morphogenesis. *Nat. Rev. Mol. Cell Biol.* **1**, 91–100 (2000).
12. L. Ding *et al.*, Genome remodelling in a basal-like breast cancer metastasis and xenograft. *Nature* **464**, 999–1005 (2010).
13. N. A. Najor, Desmosomes in human disease. *Annu. Rev. Pathol.* **13**, 51–70 (2018).
14. C. Bierkamp, K. J. McLaughlin, H. Schwarz, O. Huber, R. Kemler, Embryonic heart and skin defects in mice lacking plakoglobin. *Dev. Biol.* **180**, 780–785 (1996).
15. K. Sundfeldt, Cell-cell adhesion in the normal ovary and ovarian tumors of epithelial origin; an exception to the rule. *Mol. Cell. Endocrinol.* **202**, 89–96 (2003).
16. E. Lozano, M. Betson, V. M. Braga, Tumor progression: Small GTPases and loss of cell-cell adhesion. *Bioessays* **25**, 452–463 (2003).
17. N. Khalilgharibi *et al.*, Stress relaxation in epithelial monolayers is controlled by the actomyosin cortex. *Nat. Phys.* **15**, 839–847 (2019).
18. R. Maiti *et al.*, In vivo measurement of skin surface strain and sub-surface layer deformation induced by natural tissue stretching. *J. Mech. Behav. Biomed. Mater.* **62**, 556–569 (2016).
19. M. Padala *et al.*, Mechanics of the mitral valve strut chordae insertion region. *J. Biomech. Eng.* **132**, 081004 (2010).
20. Z. He, J. Ritchie, J. S. Grashow, M. S. Sacks, A. P. Yoganathan, In vitro dynamic strain behavior of the mitral valve posterior leaflet. *J. Biomech. Eng.* **127**, 504–511 (2005).
21. C. E. Perlman, J. Bhattacharya, Alveolar expansion imaged by optical sectioning microscopy. *J. Appl. Physiol.* **103**, 1037–1044 (2007).
22. G. B. Blanchard *et al.*, Tissue tectonics: Morphogenetic strain rates, cell shape change and intercalation. *Nat. Methods* **6**, 458–464 (2009).
23. M. S. Sacks *et al.*, Surface strains in the anterior leaflet of the functioning mitral valve. *Ann. Biomed. Eng.* **30**, 1281–1290 (2002).
24. C. M. Waters, E. Roan, D. Navajas, Mechanobiology in lung epithelial cells: Measurements, perturbations, and responses. *Compr. Physiol.* **2**, 1–29 (2012).
25. S. R. Polio *et al.*, Cross-platform mechanical characterization of lung tissue. *PLoS One* **13**, e0204765 (2018).
26. A. Monemian Esfahani *et al.*, Tissue regeneration from mechanical stretching of cell-cell adhesion. *Tissue Eng. Part C Methods* **25**, 631–640 (2019).
27. G. Charras, A. S. Yap, Tensile forces and mechanotransduction at cell-cell junctions. *Curr. Biol.* **28**, R445–R457 (2018).
28. A. Singh Vishen, J. F. Rupprecht, G. V. Shivashankar, J. Prost, M. Rao, Soft inclusion in a confined fluctuating active gel. *Phys. Rev. E* **97**, 032602 (2018).

29. N. Khalilgharibi, J. Fouchard, P. Recho, G. Charras, A. Kabla, The dynamic mechanical properties of cellularised aggregates. *Curr. Opin. Cell Biol.* **42**, 113–120 (2016).
30. X. Liang, M. Michael, G. A. Gomez, Measurement of mechanical tension at cell-cell junctions using two-photon laser ablation. *Bio Protoc.* **6**, e2068 (2016).
31. D. T. Tambe *et al.*, Collective cell guidance by cooperative intercellular forces. *Nat. Mater.* **10**, 469–475 (2011).
32. J. N. Jodoin *et al.*, Stable force balance between epithelial cells arises from F-actin turnover. *Dev. Cell* **35**, 685–697 (2015).
33. C. Bertocchi *et al.*, Nanoscale architecture of cadherin-based cell adhesions. *Nat. Cell Biol.* **19**, 28–37 (2017).
34. J. L. Bays *et al.*, Vinculin phosphorylation differentially regulates mechanotransduction at cell-cell and cell-matrix adhesions. *J. Cell Biol.* **205**, 251–263 (2014).
35. J. L. Bays, H. K. Campbell, C. Heidema, M. Sebbagh, K. A. DeMali, Linking E-cadherin mechanotransduction to cell metabolism through force-mediated activation of AMPK. *Nat. Cell Biol.* **19**, 724–731 (2017).
36. Y. Kametani, M. Takeichi, Basal-to-apical cadherin flow at cell junctions. *Nat. Cell Biol.* **9**, 92–98 (2007).
37. R. Priya, A. S. Yap, G. A. Gomez, E-cadherin supports steady-state Rho signaling at the epithelial zonula adherens. *Differentiation* **86**, 133–140 (2013).
38. J. S. Bois, F. Jülicher, S. W. Grill, Pattern formation in active fluids. *Phys. Rev. Lett.* **106**, 028103 (2011).
39. R. Priya *et al.*, Bistable front dynamics in a contractile medium: Travelling wave fronts and cortical advection define stable zones of RhoA signaling at epithelial adherens junctions. *PLoS Comput. Biol.* **13**, e1005411 (2017).
40. J. Jurado, J. de Navascués, N. Gorfinkiel, α -Catenin stabilises Cadherin-Catenin complexes and modulates actomyosin dynamics to allow pulsatile apical contraction. *J. Cell Sci.* **129**, 4496–4508 (2016).
41. C. D. Buckley *et al.*, Cell adhesion. The minimal cadherin-catenin complex binds to actin filaments under force. *Science* **346**, 1254211 (2014).
42. K. Manibog, H. Li, S. Rakshit, S. Sivasankar, Resolving the molecular mechanism of cadherin catch bond formation. *Nat. Commun.* **5**, 3941 (2014).
43. D. L. Huang, N. A. Bax, C. D. Buckley, W. I. Weis, A. R. Dunn, Vinculin forms a directionally asymmetric catch bond with F-actin. *Science* **357**, 703–706 (2017).
44. S. Rakshit, Y. Zhang, K. Manibog, O. Shafraz, S. Sivasankar, Ideal, catch, and slip bonds in cadherin adhesion. *Proc. Natl. Acad. Sci. U.S.A.* **109**, 18815–18820 (2012).
45. L. Casares *et al.*, Hydraulic fracture during epithelial stretching. *Nat. Mater.* **14**, 343–351 (2015).
46. J. G. Laffey, B. P. Kavanagh, Ventilation with lower tidal volumes as compared with traditional tidal volumes for acute lung injury. *N. Engl. J. Med.* **343**, 812, author reply 813–814 (2000).
47. J. A. Broussard *et al.*, Scaling up single-cell mechanics to multicellular tissues - the role of the intermediate filament-desmosome network. *J. Cell Sci.* **133**, jcs228031 (2020).
48. M. Rauzi, P. Verant, T. Lecuit, P.-F. Lenne, Nature and anisotropy of cortical forces orienting *Drosophila* tissue morphogenesis. *Nat. Cell Biol.* **10**, 1401–1410 (2008).
49. H. Ahmadzadeh, D. H. Smith, V. B. Shenoy, Viscoelasticity of tau proteins leads to strain rate-dependent breaking of microtubules during axonal stretch injury: Predictions from a mathematical model. *Biophys. J.* **106**, 1123–1133 (2014).
50. M. L. Gardel, K. E. Kasza, C. P. Brangwynne, J. Liu, D. A. Weitz, Chapter 19: Mechanical response of cytoskeletal networks. *Methods Cell Biol.* **89**, 487–519 (2008).
51. J. Hu *et al.*, Size- and speed-dependent mechanical behavior in living mammalian cytoplasm. *Proc. Natl. Acad. Sci. U.S.A.* **114**, 9529–9534 (2017).
52. A. R. Harris *et al.*, Characterizing the mechanics of cultured cell monolayers. *Proc. Natl. Acad. Sci. U.S.A.* **109**, 16449–16454 (2012).
53. X. Trepast *et al.*, Effect of stretch on structural integrity and micromechanics of human alveolar epithelial cell monolayers exposed to thrombin. *Am. J. Physiol. Lung Cell. Mol. Physiol.* **290**, L1104–L1110 (2006).
54. B. H. Cumpston *et al.*, Two-photon polymerization initiators for three-dimensional optical data storage and microfabrication. *Nature* **398**, 51–54 (1999).
55. R. Yang, J. A. Broussard, K. J. Green, H. D. Espinosa, Techniques to stimulate and interrogate cell-cell adhesion mechanics. *Extreme Mech. Lett.* **20**, 125–139 (2018).
56. J. A. Broussard *et al.*, The desmoplakin/intermediate filament linkage regulates cell mechanics. *Mol. Biol. Cell*, E16-07-0520 (2017).
57. Z. Liu *et al.*, Mechanical tugging force regulates the size of cell-cell junctions. *Proc. Natl. Acad. Sci. U.S.A.* **107**, 9944–9949 (2010).
58. P. Panorchan, J. P. George, D. Wirtz, Probing intercellular interactions between vascular endothelial cadherin pairs at single-molecule resolution and in living cells. *J. Mol. Biol.* **358**, 665–674 (2006).
59. J. Fröhlich, H. König, New techniques for isolation of single prokaryotic cells. *FEMS Microbiol. Rev.* **24**, 567–572 (2000).
60. S. de Beco, C. Gueudry, F. Amblard, S. Coscoy, Endocytosis is required for E-cadherin redistribution at mature adherens junctions. *Proc. Natl. Acad. Sci. U.S.A.* **106**, 7010–7015 (2009).
61. C. K. Choi *et al.*, Actin and alpha-actinin orchestrate the assembly and maturation of nascent adhesions in a myosin II motor-independent manner. *Nat. Cell Biol.* **10**, 1039–1050 (2008).
62. Y. S. Chu *et al.*, Force measurements in E-cadherin-mediated cell doublets reveal rapid adhesion strengthened by actin cytoskeleton remodeling through Rac and Cdc42. *J. Cell Biol.* **167**, 1183–1194 (2004).
63. C. T. Lim, E. H. Zhou, S. T. Quek, Mechanical models for living cells—A review. *J. Biomech.* **39**, 195–216 (2006).
64. J. J. Muñoz, S. Albo, Physiology-based model of cell viscoelasticity. *Phys. Rev. E Stat. Nonlin. Soft Matter Phys.* **88**, 012708 (2013).
65. N. Slomka, C. W. Oomens, A. Gefen, Evaluating the effective shear modulus of the cytoplasm in cultured myoblasts subjected to compression using an inverse finite element method. *J. Mech. Behav. Biomed. Mater.* **4**, 1559–1566 (2011).
66. R. Waugh, M. Tsai, *Cell Mechanics and Cellular Engineering* (Springer, 1994), pp. 33–44.
67. S. Marion, N. Guillen, J.-C. Bacri, C. Wilhelm, Acto-myosin cytoskeleton dependent viscosity and shear-thinning behavior of the amoeba cytoplasm. *Eur. Biophys. J.* **34**, 262–272 (2005).
68. A. Nikoubashman, M. P. Howard, Equilibrium dynamics and shear rheology of semi-flexible polymers in solution. *Macromolecules* **50**, 8279–8289 (2017).
69. P. Panorchan *et al.*, Single-molecule analysis of cadherin-mediated cell-cell adhesion. *J. Cell Sci.* **119**, 66–74 (2006).
70. W. E. Thomas, Understanding the counterintuitive phenomenon of catch bonds. *Curr. Nanosci.* **3**, 63–77 (2007).
71. W. R. Legant *et al.*, Multidimensional traction force microscopy reveals out-of-plane rotational moments about focal adhesions. *Proc. Natl. Acad. Sci. U.S.A.* **110**, 881–886 (2013).
72. F. Klein *et al.*, Two-component polymer scaffolds for controlled three-dimensional cell culture. *Adv. Mater.* **23**, 1341–1345 (2011).
73. F. Klein *et al.*, Elastic fully three-dimensional microstructure scaffolds for cell force measurements. *Adv. Mater.* **22**, 868 (2010).
74. J. Friedrichs *et al.*, A practical guide to quantify cell adhesion using single-cell force spectroscopy. *Methods* **60**, 169–178 (2013).
75. S. Vedula *et al.*, Quantifying forces mediated by integral tight junction proteins in cell–cell adhesion. *Exp. Mech.* **49**, 3–9 (2009).
76. H. Tabdili *et al.*, Cadherin-dependent mechanotransduction depends on ligand identity but not affinity. *J. Cell Sci.* **125**, 4362–4371 (2012).
77. C. Franz, P.-H. Puech, Atomic force microscopy: A versatile tool for studying cell morphology, adhesion and mechanics. *Cell. Mol. Bioeng.* **1**, 289–300 (2008).
78. K. E. Cavanaugh, M. F. Staddon, S. Banerjee, M. L. Gardel, Adaptive viscoelasticity of epithelial cell junctions: From models to methods. *Curr. Opin. Genet. Dev.* **63**, 86–94 (2020).
79. T. Wyatt, B. Baum, G. Charras, A question of time: Tissue adaptation to mechanical forces. *Curr. Opin. Cell Biol.* **38**, 68–73 (2016).
80. M. L. McCain, H. Lee, Y. Aratyn-Schaus, A. G. Kléber, K. K. Parker, Cooperative coupling of cell-matrix and cell-cell adhesions in cardiac muscle. *Proc. Natl. Acad. Sci. U.S.A.* **109**, 9881–9886 (2012).
81. K. V. Iyer, R. Piscitello-Gómez, J. Pajmans, F. Jülicher, S. Eaton, Epithelial viscoelasticity is regulated by mechanosensitive E-cadherin turnover. *Curr. Biol.* **29**, 578–591.e575 (2019).



Supplementary Information for

Characterization of the Strain Rate-Dependent Mechanical Response of Single Cell-Cell Junctions

Amir Monemian Esfahani, Jordan Rosenbohm, Bahareh Tajvidi Safa, Nickolay V. Lavrik, Grayson Minnick, Quan Zhou, Fang Kong, Xiaowei Jin, Eunju Kim, Ying Liu, Yongfeng Lu, Jung Yul Lim, James K. Wahl, Ming Dao, Changjin Huang, Ruiguo Yang

Nickolay V. Lavrik

Email: lavriknv@ornl.org

Ming Dao

Email: mingdao@mit.edu

Changjin Huang

Email: cjhuang@ntu.edu.sg

Ruiguo Yang

Email: ryang6@unl.edu

This PDF file includes:

Supplementary text

Figures S1 to S14

Tables S1

Legends for Movies S1 to S4

Other supplementary materials for this manuscript include the following:

Movies S1 to S4

Supplementary Information Text and Figures

1. System configuration

We used the AFM setup as a tool to stretch the platform. Specifically, we utilized its precise X, Y, and Z positioning capabilities to capture the pillar on the device within a hole drilled into the tip of a cantilever probe tip, and could subsequently define a path for the tip to follow at a specified speed to apply strain at a controlled strain rate to the platform. We did not use any other functions such as spectroscopy. To help illustrate how the AFM setup is integrated into our platform, we drew a Solidworks model as shown in **Fig. S1**.

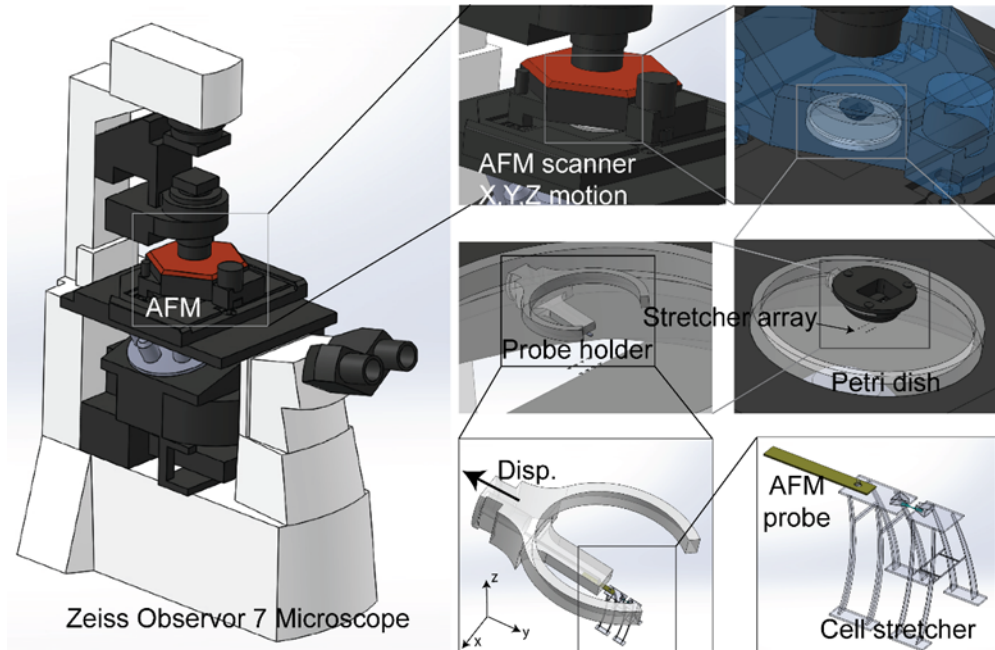


Fig. S1. Detailed illustration of the entire SCA μ TT platform. An AFM probe with a hole drilled in the tip with a focused ion beam (FIB) is mounted on the scanner head, and the AFM system is then placed on the stage of an inverted microscope above the sample. The probe tip is then moved using controls on the stage and the AFM software until the pillar is captured within the hole on the probe tip. From here, a line for the probe tip to follow is defined within the AFM software along with the scanning speed to displace the tip in the Y-direction and apply the strain at a controlled strain rate.

2. Design, simulation, and fabrication of the single cell stretcher structure

Several generations of the sensing beam structure have been designed, fabricated, and tested, and their stiffness was calculated using COMSOL Multiphysics simulation software. The first generation was a group of parallel horizontal beams. A design with 5 sets of beams was proposed as the first design. After the simulation, the calculated stiffness was $K = 1e5$ N/m, which, compared to biological samples, was too large to measure the stress in the cell-cell junction (**Fig. S2a**). By reducing the number of beams, decreasing the beam width from $5\ \mu\text{m}$ to $2.5\ \mu\text{m}$, and increasing the beam length from $80\ \mu\text{m}$ to $150\ \mu\text{m}$, we were able to decrease the stiffness to 4.6 N/m (**Fig. S2b**). However, this was still too large to measure stress. Since we reached the maximum printing dimensions of the 3D printer device without stitching, we could not increase the length and due to the structure stability, we could not decrease the width of the beams. A serpentine beam was then proposed to further decrease the stiffness with these geometric constraints in mind. This design further reduced the stiffness of the structure ($K = 1.05$ N/m) but was still too stiff. (**Fig. S2c**). The force-displacement curves of these designs are compared in **Fig. S2d**. It is worth mentioning that these stiffness data are all calculated in air.

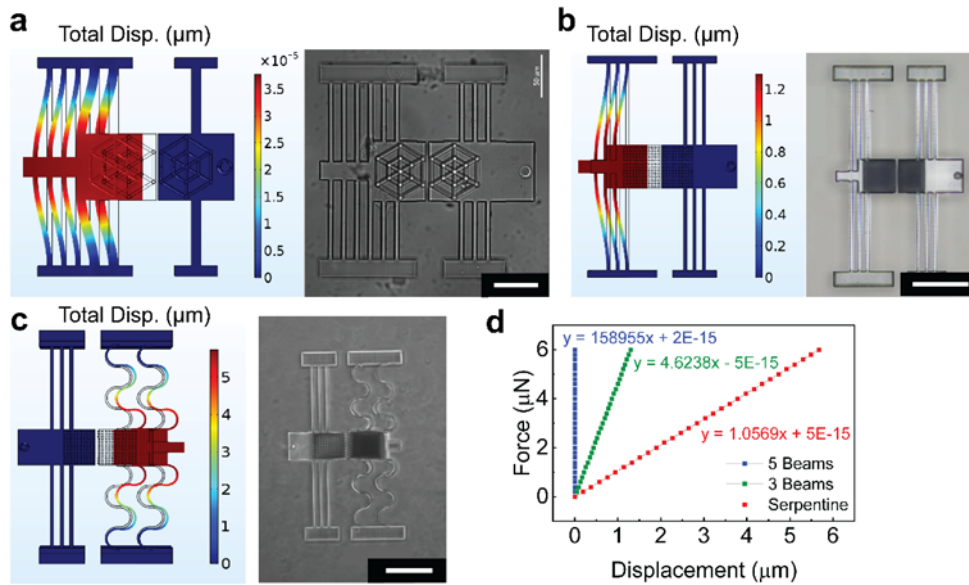


Fig. S2. Design, simulation, and fabrication of the first generation of the single cell pair stretcher (horizontal). **a.** Horizontal beam design with 5 parallel beams attached to the sensing island and 1 pair of beams attached to the actuating island. This design had the highest stiffness ($K = 1e5$ N/m) and was not able to measure the junction stress. Scale bar = $50\ \mu\text{m}$. **b.** Horizontal beam design with 3 pairs of beams attached to the sensing and actuating islands, with the width decreased from $5\ \mu\text{m}$ to $2.5\ \mu\text{m}$ and length increased from $80\ \mu\text{m}$ to $150\ \mu\text{m}$. The new stiffness was 4.6 N/m which is not low enough to measure the junction stress. Scale bar = $100\ \mu\text{m}$. **c.** Horizontal beam design in which the sensing island beams are changed from the straight to the serpentine design which is less stiff. This design had 1.05 N/m stiffness which is still too stiff to measure the junction stress. Scale bar = $100\ \mu\text{m}$. **d.** The force versus displacement of different designs has been plotted to compare and find their stiffness.

All of the horizontal beam designs have a stiffness higher than our desired values (0.01 N/m – 0.5 N/m). So, a vertical beam design was proposed (**Fig. S3a**). The vertical beam with a height of $280\ \mu\text{m}$ was able to give us a stiffness close to our goal (0.22 N/m). However, the beams being exactly underneath the islands creates high-intensity background noise during fluorescent imaging, blocking the signal from cells. Therefore, we designed a double cantilever beam design by moving the beams' bases to the sides of the islands (single Λ -shape). Theoretically, this change resulted in increasing the stiffness, so the design was modified by decreasing the beam thickness from $5\ \mu\text{m}$ to $2.5\ \mu\text{m}$ and increasing its height to $300\ \mu\text{m}$. With COMSOL simulation, its stiffness is lower than the other beam geometry designs (0.08 N/m); however, it collapsed during fabrication. Adding

another set of Λ -shape beams (double Λ -shape) to increase stability still resulted in the collapse of the structures (**Fig. S3b**). Finally, a set of trusses were added horizontally to connect the vertical beams and enhance stability (stabilized A-shape), while decreasing the beam thickness to $2\ \mu\text{m}$, resulting in stable structures with a stiffness of $0.11\ \text{N/m}$. (**Fig. S3c, d**). It is worth mentioning that these stiffness data are all calculated in air.

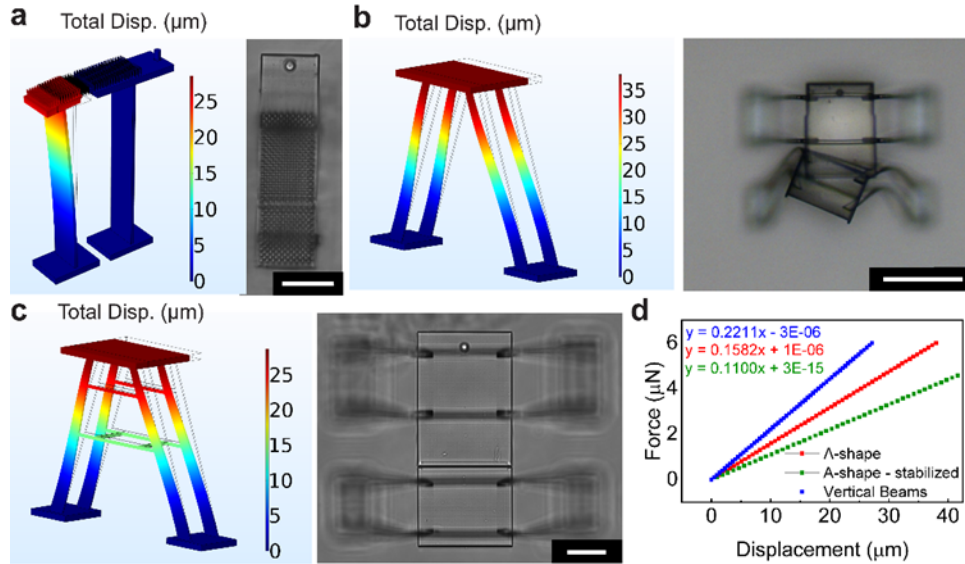


Fig. S3. Design, simulation, and fabrication of the second generation of the single cell pair stretcher (vertical). **a.** The vertical beam design was less stiff compared to the horizontal beam design and more stable during fabrication. The new design had a height of $280\ \mu\text{m}$ and its stiffness was $0.22\ \text{N/m}$, which allows us to measure the junction stiffness. Scale bar = $50\ \mu\text{m}$. **b.** The double Λ -shape design solved the background noise issue but it was not stable during fabrication and collapsed. Scale bar = $100\ \mu\text{m}$. **c.** The double A-shape design with the supporting truss was the final design because of its stiffness and stability. Scale bar = $50\ \mu\text{m}$. **d.** The force versus displacement of the vertical beam designs has been plotted to compare and find their stiffness.

3. Beam stiffness calculation and calibration

To measure the cell-cell adhesion forces, the mechanical characteristics of the sensing mechanism must be well understood. The modulus of elasticity of TPP fabricated materials varies with laser power, print speed, and post process curing methods. In this study, fabrication parameters remained as consistent as possible. This section highlights the methods used to test, calibrate, and verify the stiffness of the sensing structure mechanism to determine the adhesion forces associated with cell stretching. To do this, a Nanosurf AFM was used to conduct force spectroscopy experiments on horizontally printed sensing microstructures to attain an average stiffness value.

As mentioned in the paper, a tipless cantilever probe (TL-NCL by Nanosensors) with a known and thermally tuned stiffness, k_p , was used to press on horizontally fabricated sensing microstructures with beam thickness, $t = 2 \mu m$ (**Fig. 1e**). AFM uses the deflection of the probe, Δx_p , and its known stiffness, k_p , to measure the applied force, P_{AFM} . The sensing microstructure is also subjected to the same force as it produces the reaction to cause the probe deflection:

$$P_{AFM} = \Delta x_p \cdot k_p = \Delta x_{sens} \cdot k_{sens} \quad (S1)$$

Here, Δx_{sens} and k_{sens} are the deflection and stiffness of the sensing microstructure, respectively. The AFM outputs the data as force, P_{AFM} , versus displacement, d (**Fig. 1f**). As shown in **Fig. 1e**, the probe is deflected upwards and the structure downwards, therefore the deflection of the microstructure can be calculated by the following:

$$\Delta x_{sens} = d - \Delta x_p \quad (S2)$$

To evaluate the data to find the stiffness, the probe deflection is first found from Eqn. (S1). Next, the structure deflection is solved using Eqn. (S2). Lastly, by substituting the values into the sensing part of Eqn. (S1), the stiffness can be found:

$$k_{sens} = \frac{P_{AFM}}{\Delta x_{sens}} = \frac{1}{d/P_{AFM} - 1/k_p} \quad (S3)$$

To analyze the AFM data, a MATLAB script was used to smooth and average the AFM force versus deflection curves and to calculate the sensing structure stiffness by fitting the averaged line of the data, where the slope was equal to the stiffness.

4. Elastic deformation of the structure

To examine the elasticity of the structure, two experiments were performed with a controlled displacement and release. The first one was a 25 μm displacement and sudden release of the structure and the second one was a 50 μm displacement and sudden release. Since lower strain rates have more impact on the viscoelastic properties of the material, we used 100 nm/s (0.005 s^{-1}) for both experiments. **Fig. S4** shows the displacement-time plots for the experiments. For the 25 μm displacement, 0.135 seconds after release, and for the 50 μm displacement, after 4.72 seconds, both return to the original position within the resolving power of the DIC, thus ruling out major plastic deformation. Further, the rapid release and return of the 25 μm test demonstrate that the viscoelastic effect can be negligible with this displacement, slightly less so with the 50 μm test. In our cell stretch experiments, the displacement of the sensing island is within 5 μm , in which elastic deformation dominates according to this experiment.

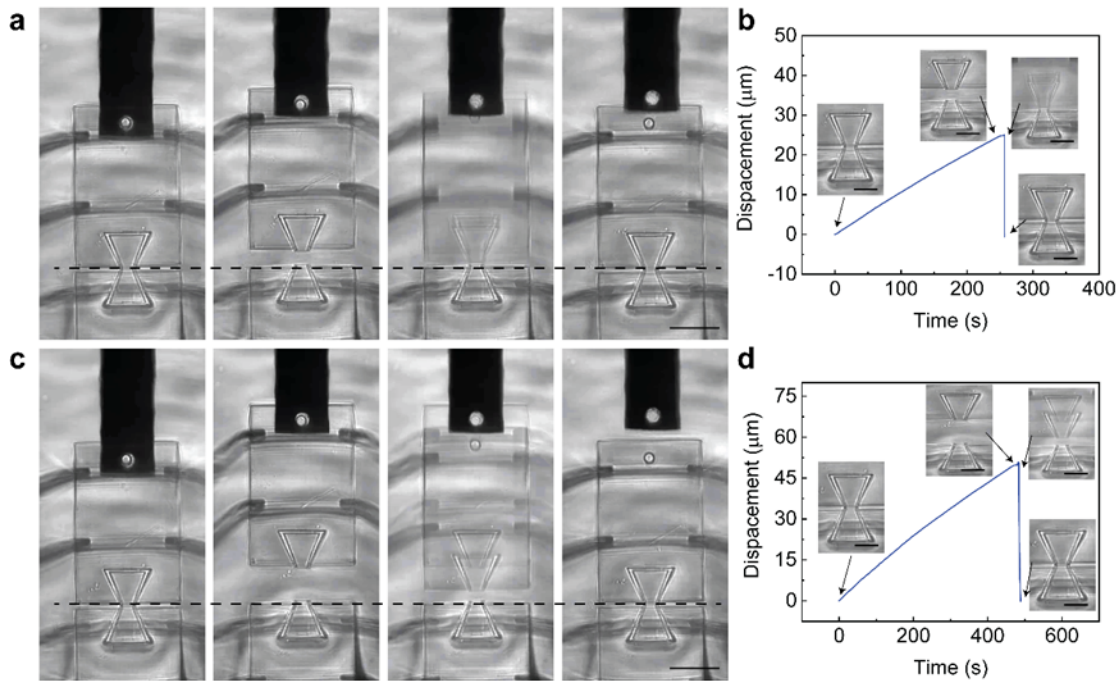


Fig. S4. Elastic deformation of the structure. a. 25 μm displacement and sudden release. Scale bar: 50 μm . b. Displacement versus time for the 25 μm displacement. Scale bar: 25 μm . c. 50 μm displacement and sudden release. Scale bar: 50 μm . d. Displacement versus time for the 50 μm displacement. Scale bar: 25 μm .

5. Cell deposition procedure

Cell manipulation was performed using the well-known Eppendorf cell isolation system. This setup consists of a microcapillary (Piezo Drill Tip ICSI, Eppendorf) integrated with a pressure controller (CellTram® 4r Air/Oil, Eppendorf) and a 3D manipulator (TransferMan® 4r, Eppendorf), allowing for precise 3D cell manipulation. The inner diameter of the microcapillary was chosen based on the cell diameter (approximately 15 μm). To aspirate and hold a cell on the needle tip, the inner diameter should be less than the cell diameter. Based on available needle sizes from Eppendorf, we selected Piezo Drill Tip ICSI with 6 μm inner diameter. The needle is connected to the capillary and through a tube to the pressure controller. The tube is filled with mineral oil, and a small displacement of the pressure controller cylinder creates a positive or negative pressure at the needle tip. The needle approaches the cell using the 3D manipulator (**Fig. S5a**). When it touches the cell membrane, a negative pressure is applied to aspirate the cell (**Fig. S5b**). While the cell is held at the needle tip, it is positioned above Island 2, and a positive pressure is applied to detach the cell from the needle and place it on the surface (**Fig. S5c**). The same procedures are performed to place the second cell on Island 1 (**Fig. S5d, e, and f**). This process is performed inside a temperature-controlled chamber.

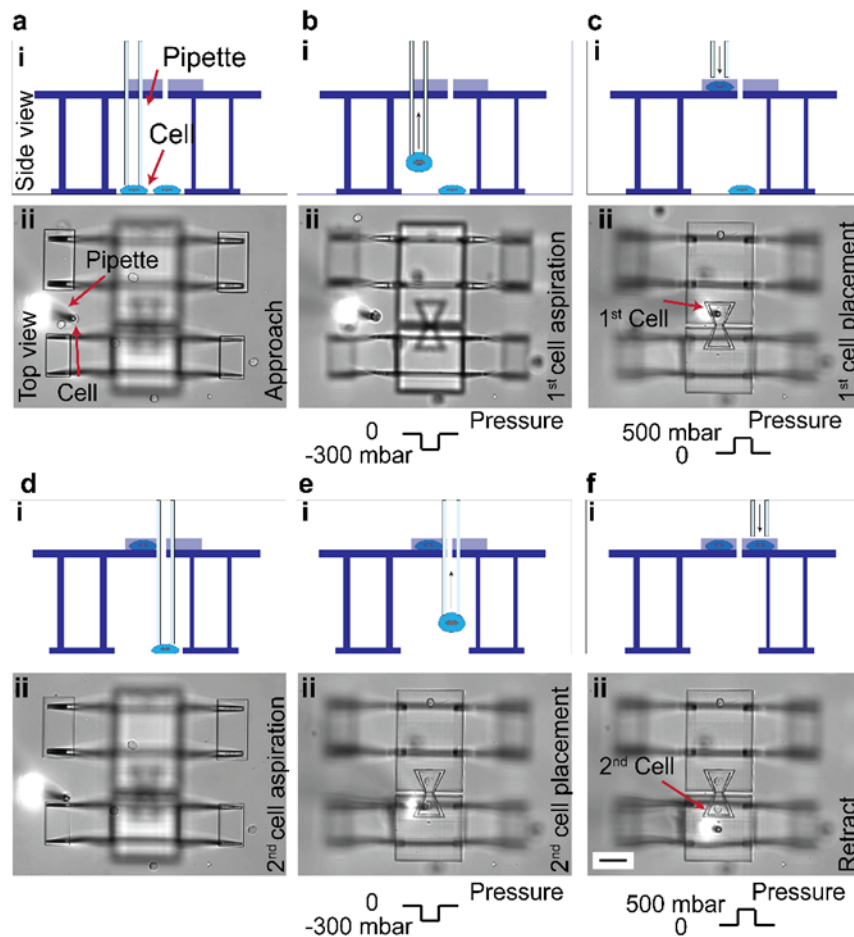


Fig. S5. Cell deposition procedure. a. One cell is targeted and the microcapillary approaches the cell using the 3D manipulator. b. A negative pressure is applied with the pressure controller to aspirate and hold the cell. c. The manipulator moves the cell to the structure and a positive pressure is applied to deposit the cell on one of the islands. d-f. The same steps are performed to aspirate and deposit the second cell on the other island.

6. Cell-cell junction separation under stretch test

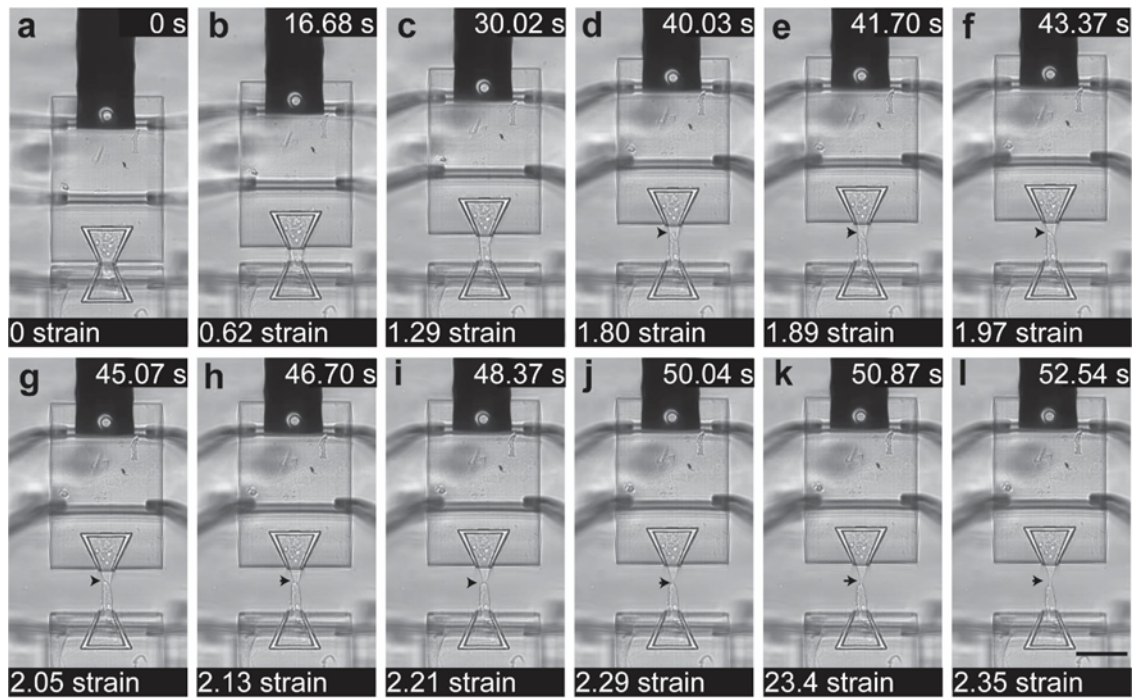


Fig. S6. A representative time-lapse series of frames show the cell junction ruptured symmetrically under an increasing strain. The arrowhead indicates the cell-cell junction in each frame. Scale bar: 20 μm .

7. Standard linear solid model fitting

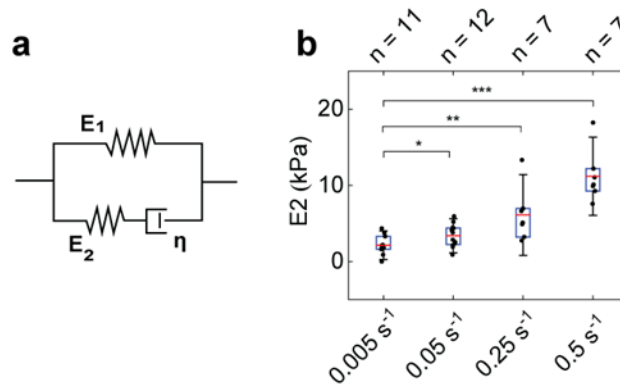


Fig. S7. Fitting the stress-strain curves with the Standard Linear Solid (SLS) model. **a.** Diagram of the SLS model. **b.** The predicted spring constant E_2 as a function of the strain rate. The equation for the SLS model: $\dot{\sigma}_{tot} + \frac{E_2}{\eta} \sigma_{tot} = \frac{E_1 E_2}{\eta} \varepsilon_{tot} + (E_1 + E_2) \dot{\varepsilon}_{tot}$ can be solved for a constant strain rate: $\sigma_{tot} = \eta \dot{\varepsilon}_{tot} (1 - e^{-\frac{E_2 t}{\eta}}) + E_1 \varepsilon_{tot}$. This equation was used to fit the stress-strain curves at strain rates: 0.005 s⁻¹, 0.05 s⁻¹, 0.25 s⁻¹ and 0.5 s⁻¹. The fitting curves are similar to the ones with MSLS fitting in Figure 4b-c. The fitting process yields a relationship between E_2 and strain rate in (b), which shows Young's modulus of the intracellular components, primarily the cytoskeleton, increases significantly with the increase in strain rate. This prediction is clearly in contradiction to the fact that cytoskeleton growth is limited in tests at high strain rates due to the limited response time.

8. CN01, control DMSO, and bleb stretch test frames

Investigation of cellular contractility was performed using CN01, control DMSO, and Bleb with a 0.005 s^{-1} (100 nm/s) strain rate, and representative frames are shown in **Fig. S8**. Control DMSO compared to control at 0.005 s^{-1} showed a sign of rupture because of DMSO (**Fig. S8a**). CN01 increased the stress level and rupture did not occur in this test (**Fig. S8b**). Since Bleb inhibits the myosin II pathway, the cell-cell adhesion junction ruptured at the initial stages and the stress level was low compared to other conditions (**Fig. S8c**).

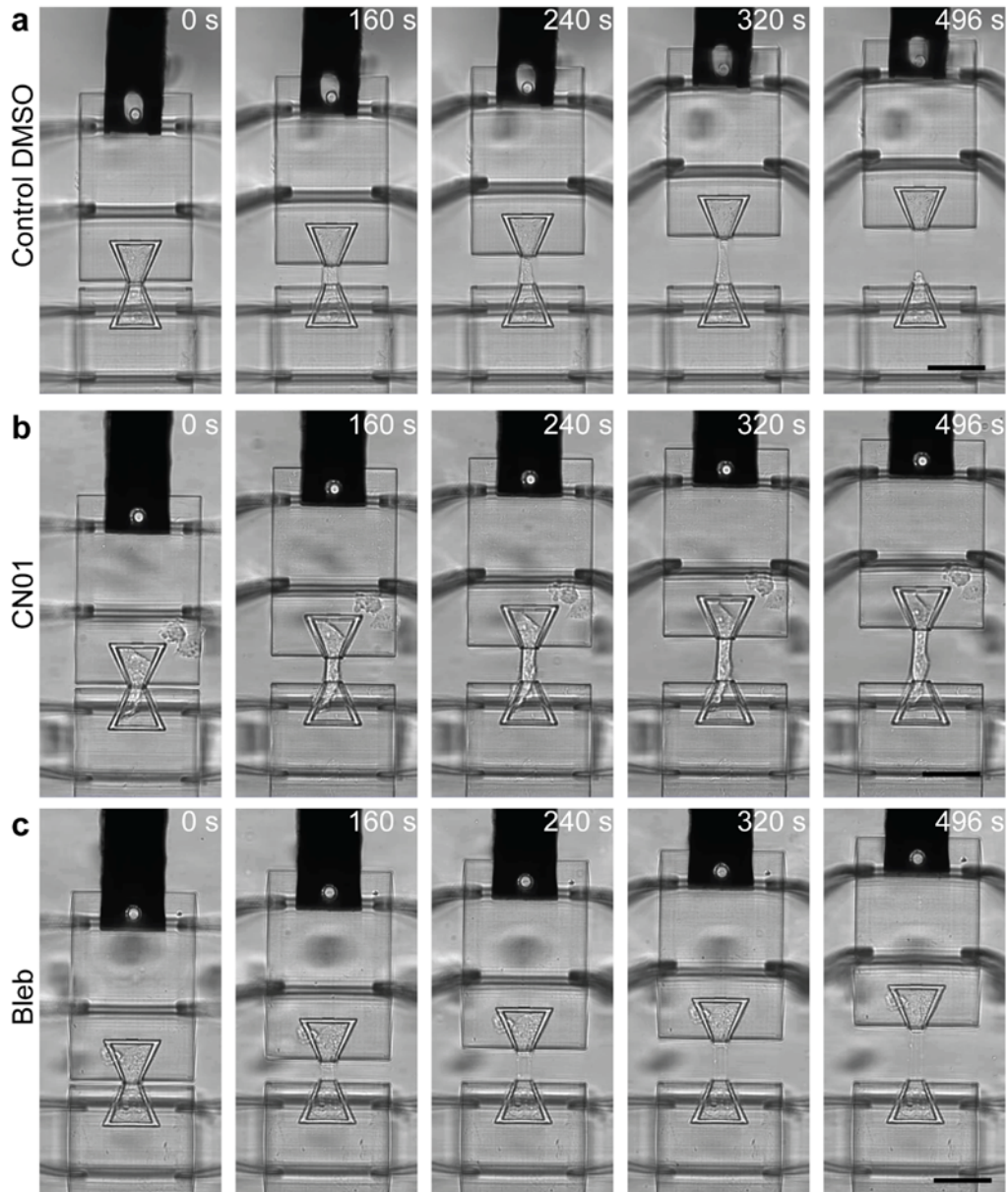


Fig. S8. Series of frames for CN01, control, and bleb under 0.005 s^{-1} strain rate stretch test. a. Control DMSO. b. CN01. c. Bleb. Scale bar: $50 \mu\text{m}$.

9. Stress modulation reversal by sequential addition of contractility modulators

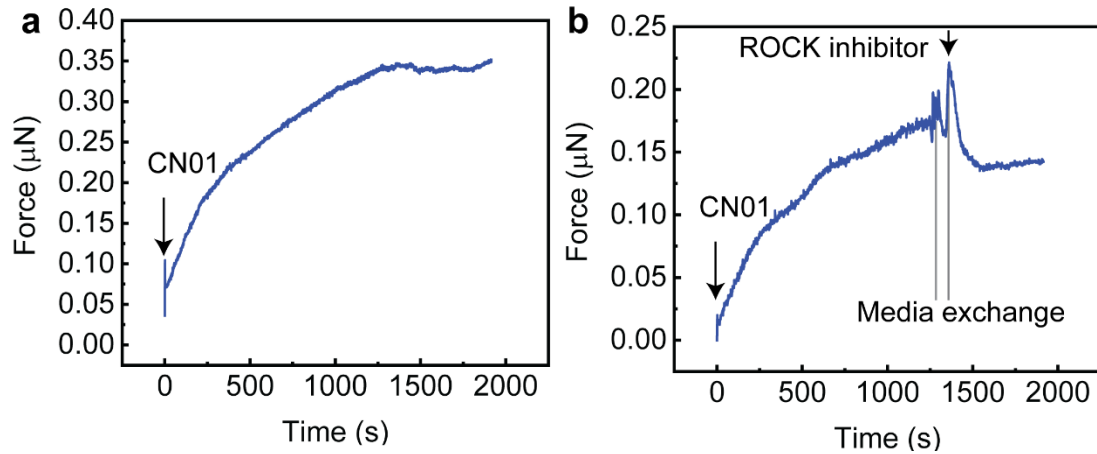


Fig. S9. Reversal of the stress modulation effect of a RhoA activator by ROCK inhibitor. a. Temporal evolution of the force sustained by a cell pair in response to CN01 (1 unit/ml) while maintaining a constant strain of 0.5. **b.** Temporal evolution of the force sustained by a cell pair in response to sequential addition of CN01 (1 unit/ml) and ROCK inhibitor while maintaining a constant strain of 0.5.

10. Cell-cell adhesion junction length calculation

To calculate the junction length, ImageJ (NIH funded software) was used. The scale is assigned to the frames of interest and a freehand line was drawn on the junction. By analyzing these lines through the software, each length can be measured and tabulated (Fig. S10).

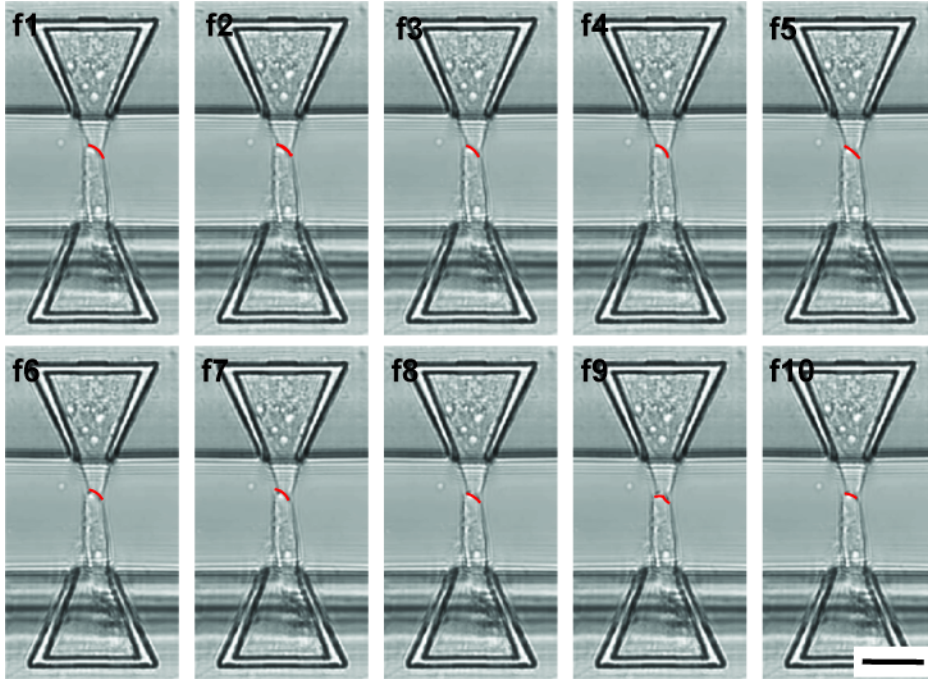


Fig. S10. Cell-cell adhesion junction length calculation. The cell-cell adhesion junction lengths were calculated using ImageJ software. After defining the scale for each frame, a freehand line was drawn on the junction and its length was captured (f1 to f10). Scale bar: 25 μm .

Table S1. Junction length measurement on the frames in Fig. S10.

Frame #	Junction length (μm)
1	8.019
2	7.889
3	7.931
4	7.673
5	7.043
6	6.698
7	6.121
8	5.789
9	5.513
10	5.147

11. Cadherin bond clustering in cell-cell junction under mechanical strain

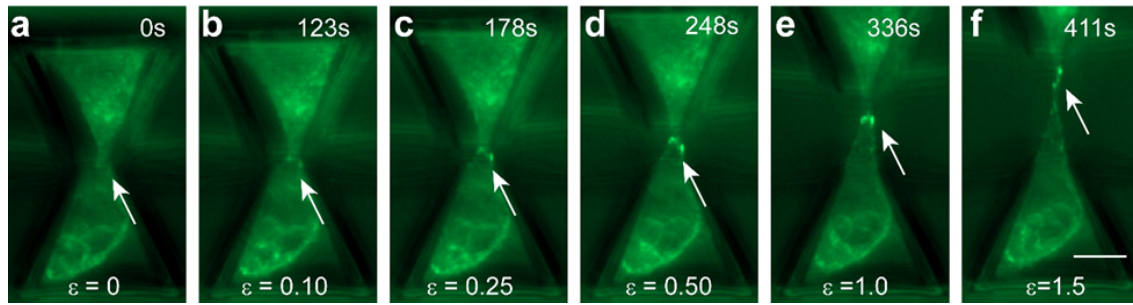


Fig. S11. E-cadherin clustering in cell-cell junction under applied strain. **a.** Under 0% strain, A431 GFP-tagged E-cadherin cells have a little expression of E-cadherin at cell-cell junction. **b-e.** As strain is increased to 10%, 25%, 50%, and 100%, respectively, E-cadherin signal increases at the cell-cell junction, indicating clustering of E-cadherin in response to stretch. **f.** At 150% strain E-cadherin begins to retract from the cell-cell contact. Scale bar: 20 μm .

12. E-Cadherin siRNA knockdown

To determine the E-cadherin bond effect on the stress-strain curve and bond rupture initiation, E-cadherin siRNA was transfected into A431 GFP-tagged E-cadherin cells. Cells were incubated with control siRNA and E-cadherin siRNA both using the Lipofectamine RNAiMAX reagent. The inhibition of E-cadherin expression was confirmed by fluorescence microscopy and immunoblotting. A knockdown of E-cadherin expression could be visualized by fluorescence microscopy after 48 h transfection. Also, immunoblotting showed that the protein levels of E-cadherin were dramatically decreased in the E-cadherin siRNA samples (48 h, 72 h, and 96 h) compared to control siRNA. These results show that E-cadherin siRNA downregulated the E-cadherin expression effectively. Note, since we used A431 cells having GFP-tagged E-cadherin, the immunoblotting showed two bands for endogenous E-cadherin (120 kDa) and GFP-tagged E-cadherin (at around 150 kDa due to the addition of GFP of 27 kDa). The control siRNA sample displayed the same two bands, and E-cadherin siRNA induced decreases in both bands. Tensile test data (Fig. 5f-h) compared between the control siRNA and E-cadherin siRNA.

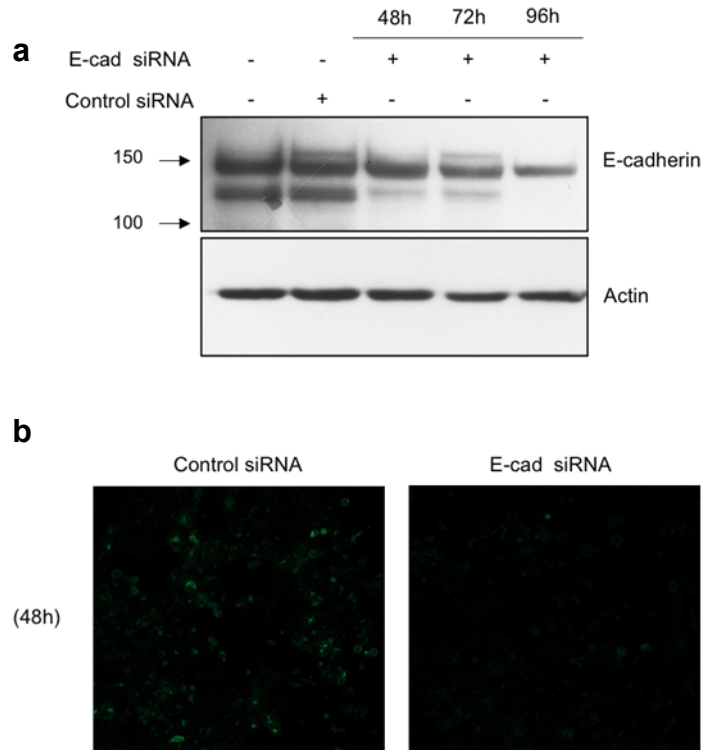


Fig. S12. Confirmation of E-cadherin siRNA silencing. **a.** A431 GFP-tagged E-cadherin cells were transfected with control siRNA or E-cadherin siRNA. After 48 h, 72 h, and 96 h post-transfection with E-cadherin siRNA, expression levels of E-cadherin were decreased in both endogenous E-cadherin (120 kDa) and GFP-tagged E-cadherin (at around 150 kDa), as assessed by immunoblot. Actin levels were not affected by the siRNA transfection. **b.** GFP signal in GFP-tagged E-cadherin A431 cells was observed after 48 h transfection with control siRNA and E-cadherin siRNA by immunofluorescence.

13. Cell-cell junction length, thickness, and nucleus-to-nucleus distance

The length of the junction is determined by measuring the length of the cell-cell contact with GFP-tagged E-cadherin, the nucleus-to-nucleus distances are calculated by examining the center-of-mass for the nucleus DAPI staining, and the thickness of cell-cell junctions are measured by examining the z-stack images of a single junction on a TPP-printed scaffold to determine the number of images in which the junction is in focus.

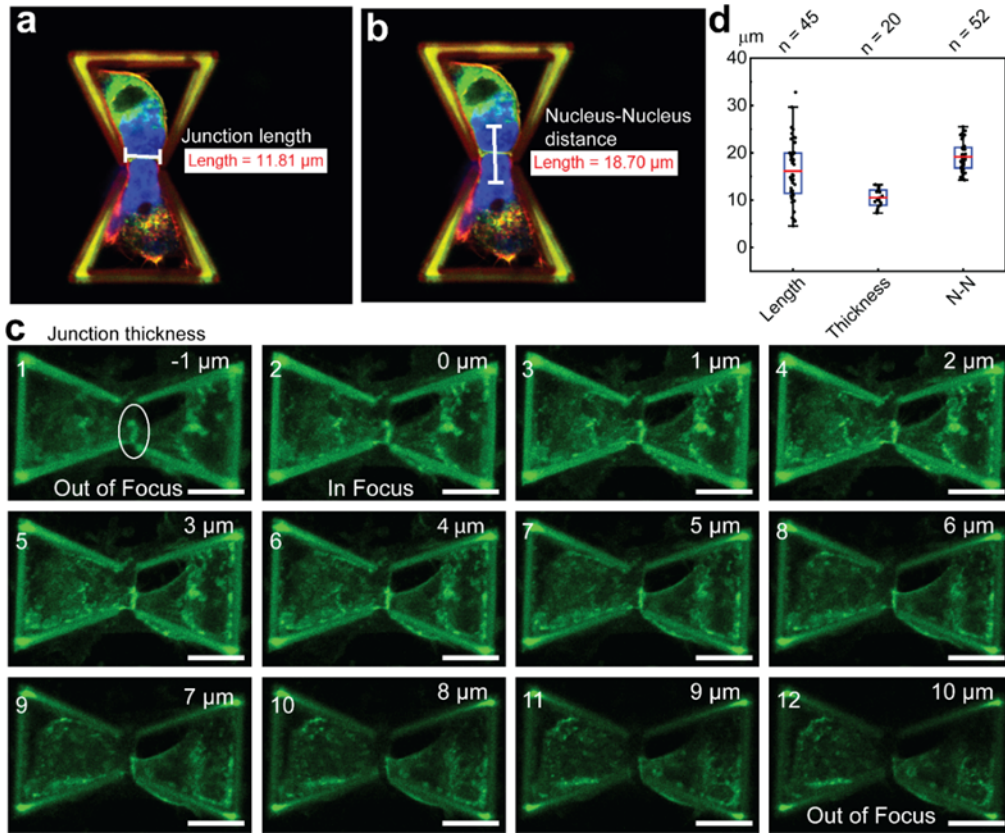


Fig. S13. Cell-cell junction dimension quantification and analysis. **a, b.** A cell pair adhered well on the device with a cell-cell junction within the gap. The junction length was measured through the junction line which is determined with the GFP-tagged E-cadherin. The nucleus-to-nucleus distances are examined by DAPI staining. **c.** Z-stack images of a cell-cell junction for thickness measurement (scale bar = 20 μm). To determine the junction thickness, cells were deposited in bowtie structures and allowed to form junctions overnight. Then, z-stack images were taken of each bowtie structure with a cell-cell pair with a spacing of 1 μm between each image. To find the thickness of the junction, the image with the bottom of the junction in focus was determined, and then each image after was examined until the top of the junction was just out of focus. From here the thickness was determined based on the number of images between these identified images (from 2 to 12). Based on the new values, we changed our assumption for the junction area in stress calculation and recalculated all previous data. **d.** Cell-cell junction length, thickness, and the nucleus-to-nucleus distance were measured and plotted (n = 45 for junction length measurements, n = 20 for thickness measurements, and n = 52 for nucleus-to-nucleus (N-N) distance measurements).

14. Initial length for strain calculation

We chose to define the initial length as the distance between the nuclei based on some observations during the stretching process. We observed that regions of the cell nearest to the junction deformed the most, while regions behind the nucleus remained relatively unmoved. To show that the region behind the nucleus is almost intact during the stretch test, we analyzed the change in displacement of a distinctive spot as a marker with respect to the edge of the bowtie, $L_M(t)$, and compared it with the displacement difference of the two movable islands, $L(t)$. As shown by the representative frames of a stretch test example, the marker, approximately in the region of the cell nucleus, was displaced only slightly from its original position relative to the edge of the bowtie ($L_M(0)$) and the maximum $L_M(t)$ reaches only $1.8\ \mu\text{m}$ as compared to the maximum of $L(t)$ at $47.5\ \mu\text{m}$. Therefore, we assumed that the cell is fully anchored behind the nucleus, and while there may be some adhesions on the side near the junction, the majority of the deformation happens in this region, and these adhesions are most likely ruptured first, making this assumption more accurate. We do understand this assumption is not perfect and that there are a number of confounding factors to introduce error into the strain calculation. However, under large deformation (as the deformation of the cell pair during the stretch can reach several folds of the initial length), the influence of these errors on the calculated stress-strain relationships is mitigated.

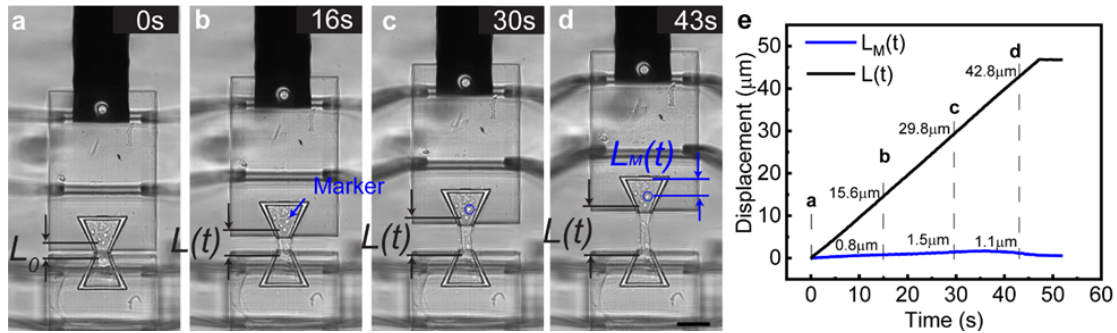


Fig. S14. Initial length calculation. a-d. Selected frames from an example stretch test showing the displacement of the upper island with respect to the lower island, $L(t)$, and the displacement of a marker close to the nucleus of the cell on the upper island with respect to the edge of the bowtie, $L_M(t)$. e. Plot of the displacement change over the course of the stretch test for $L(t)$ and $L_M(t)$. Scale bar = $20\ \mu\text{m}$.

Supplemental video captions:

Movie S1 (separate file).

Video recordings for the stretch test shown in Figure 3 a-b in the main text

Movie S2 (separate file).

Video recordings for the stretch test shown in Figure 3 c-d in the main text

Movie S3 (separate file).

Video recordings for the stretch test shown in Figure 3 e-f in the main text

Movie S4 (separate file).

Video recordings for the stretch test shown in Figure 3 g-h in the main text